Integrated Master in Chemical Engineering

Production of green fuel additives assisted by supercritical carbon dioxide

Master's Dissertation

by

Pedro Monteiro Walgode

Developed within the course of dissertation at:

LSRE - Laboratory of Separation and Reaction Engineering

Supervisor at FEUP:

Dr. Rui Pedro Vieira Faria

Dra. Ana Mafalda Almeida Peixoto Ribeiro

Prof. Alírio Egídio Rodrigues

Department of Chemical Engineering

November of 2017

Agradecimentos

Esta dissertação é o encerrar de um ciclo, mas com certeza não é um ponto final na história. Novas e vindouras oportunidades surgirão, pois só janelas se poderão abrir com o fechar desta porta.

Antes de mais, à minha mãe, à minha irmã e ao meu pai, um sentido obrigado! Vocês são o meu pilar e sem vocês não seria o homem que hoje sou.

Aos meus orientadores, Rui Pedro e Ana Mafalda, expresso a minha gratidão, vocês foram incansáveis. A vossa alegria e disponibilidade tornam o trabalho muito mais estimulante, interessante e gratificante. Convosco aprendi imenso, é um prazer trabalhar assim!

Aos meus amigos, família que escolhi e que levo para a vida, a vós agradeço por me acompanharem, ajudarem e por poder partilhar convosco esta viagem.

Por fim, agradeço a todos os colegas de curso que me acompanharam ao longo destes ultimos cinco anos e me ajudaram a terminar o mestrado com sucesso.

Este trabalho foi financiado pelo projeto POCI-01-0145-FEDER-006984 - Laboratório Associado LSRE-LCM e pelo projeto PTDC/QEQ-ERQ/2698/2014 – POCI-01-0145-FEDER-016866- financiados pelo Fundo Europeu de Desenvolvimento Regional (FEDER), através do COMPETE2020 – Programa Operacional Competitividade e Internacionalização (POCI) e por fundos nacionais através da Fundação para a Ciência e a Tecnologia I.P (FCT).

“Que seja infinito enquanto dure.”

Vinicius de Moraes

Resumo

O crescimento da indústria do biodiesel, setor das energias renováveis, está a provocar uma acumulação de "crude glycerol", produto secundário da produção de biodiesel, com valor económico praticamente nulo. É imperativo valorizar o glicerol para aumentar a sustentabilidade económica e ambiental da produção de biodiesel, sendo uma das soluções a reação do glicerol com acetona, produzindo solketal com praticamente 100% de seletividade. O solketal é um produto de elevado valor acrescentado com inúmeras aplicações, sendo a mais importante como aditivo de combustíveis. Muito trabalho tem sido desenvolvido na área de reação, testando-se inúmeros catalisadores e condições de operação. Já relativo à separação do solketal dos produtos pouco trabalho foi feito. O solketal não é ainda produzido à escala industrial, sendo preciso solucionar alguns prolemas, principalmente de transferência de massa relacionados com a elevada viscosidade do glicerol e a baixa solubilidade da acetona neste.

Neste trabalho é proposto o uso de dióxido de carbono supercrítico como solvente de separação, uma solução eficiente e ecológica de forma a ultrapassar problemas de equilíbrio e de transferência de massa e ainda com vista à utilização de correntes industriais secundárias. O adsorvente usando para a separação do solketal é o zeólito HBEA-25, um catalisador ácido para a reação de produção de solketal e ainda um agente de desidratação, removendo água do sistema e ultrapassando assim as limitações de equilíbrio reacionais. Pode assim ser usado para intensificação de processos com reação e separação na mesma unidade.

São realizadas perturbações de pulso numa coluna de leito fixo supercrítico injetando separadamente diferentes concentrações de acetona, solketal e água em dióxido de carbono supercrítico, variando a pressão entre 100 e 200 bar e a temperatura entre 313 e 353 K. Com os resultados obtidos, simulou-se um TMB em meio supercrítico para separar solketal de água.

Verificaram-se as seguinte tendências para os tempos de residência médios das perturbações de pulso: $\overline{t}_r$ acetona < $\overline{t}_r$ solketal << $\overline{t}_r$ água. Geralmente o $\overline{t}_r$ aumenta com a temperatura e diminui com a pressão, exceto a água onde $\overline{t}_r$ diminui tanto com a temperatura ou pressão.

As isotérmicas de adsorção foram descritas pelo modelo de Langmuir. Para o SF-TMB foi proposto adsorção competitiva entre o solketal e a água, testando-se os modelos de competição pura e competição "Dual Site". As condições de operação ótimas para um SF-TMB de quatro colunas obteve-se a 150 bar e 353 K, com uma pureza de extracto e de refinado de 99%, uma produtividade de 18.8 kg_{Solk}/L_{Ads}·dia e um consumo de eluente de 56.1 $L_{Des}/kg_{solketal}$ (considerando o modelo de equilíbrio de adsorção competitiva "Dual Site").

Palavras Chave: Dióxido de carbono supercrítico, Isotérmicas de adsorção de Langmuir, SF-TMB, Solketal, Zeólito HBEA-25.

Abstract

The increasing renewable energy industry, specifically biodiesel industry, is leading to an excess of crude glycerol as a reaction byproduct, with almost no economic value, which valorization becomes a priority to improve biodiesel industry economic and environmental competitiveness. A solution may be reacting it with acetone in acid media to produce solketal, a high added value product, in a reaction with almost 100% selectivity. Solketal main application is as a green fuel additive, which can be blended with biodiesel itself to improve its octane number and stability.

Although a lot of research has been done concerning the reaction catalysis, barriers to solketal economic viability and industrial scale up are still found in the proposed processes. Glycerol high viscosity and acetone very low solubility in glycerol at normal conditions are reaction obstacles that need to be overcome, as well as sustainable solketal separation processes. Solutions as reactive distillation have already been proposed, but no industrial scale process is found.

In this work, supercritical carbon dioxide is proposed as a solvent to overcome equilibrium and mass transfer problems, providing an efficient and environmentally friendly solketal separation process. It is of great importance to found useful applications to the industrial waste carbon dioxide. The adsorbent used for solketal separation is the zeolite HBEA-25, a strong acid catalyst for the solketal production reaction and a dehydrating agent, removing water from the system and overcoming the reaction equilibrium limitation. As so, it can be used in the future in process intensification with reaction and separation on the same unit.

A screening of operating conditions for acetone, solketal and water pulse experiences in a supercritical fixed bed chromatographic column was performed for different concentrations, pressures ranging from 100 to 200 bar and temperatures from 313 to 353 K. From the pulse results, a SF-TMB model was designed and simulated at three different operating conditions.

The following average residence time tendencies were found: $\overline{t}_r$ acetone < $\overline{t}_r$ solketal << $\overline{t}_r$ water. Generally $\overline{t}_r$ increases with temperature and decreases with pressure, exception goes to water where $\overline{t}_r$ decreases both with temperature and pressure. The adsorption equilibrium isotherm was successfully fitted by a Langmuir model.

For the SF-TMB, competitive adsorption for water and solketal mixture was proposed, testing pure and Dual Site competition. The four columns SF-TMB optimum was found at 150 bar and 353 K. For a minimum extract and raffinate purity of 99%, a solketal productivity of 18.8 kg_{Solk}/L_{Ads}·day and an eluent consumption 56.1 $L_{Des}/kg_{solketal}$ were obtained for Dual Site competitive model.

Keywords: Langmuir isotherm adsorption, solketal, supercritical carbon dioxide, SF-TMB, zeolite HBEA-25.

Declaração

Declara, sob compromisso de honra, que este trabalho é original e que todas as contribuições não originais foram devidamente referenciadas com identificação da fonte.

Index

1 Introduction 1

1.1 Motivation and relevance 1

1.2 Thesis outline 2

2 Context and State of the art 3

2.1 Solketal: a product of glycerol and acetone reaction 4

2.2 Supercritical fluids 5

2.3 Equilibrium data 6

2.1 Supercritical separation 9

3 Materials and Methods 11

3.1 Materials 11

3.1.1 Chemicals 11

3.1.2 Zeolite HBEA-25 12

3.2 Experimental set-up 13

3.2.1 SFC-unit 13

3.2.2 SFC-fixed bed column 14

3.3 Experimental procedure (pulse experiments) 15

3.4 Mathematical modelling 16

3.4.1 SFC-fixed bed 16

3.4.2 TMB 18

3.5 $ScCO_2$ properties and correlations 22

4 Results and Discussion 25

4.1 Pulse experiments 25

4.2 Parameter estimation 30

4.3 TMB simulation 36

5 Conclusions 43

5.1 Objectives Achieved 43

5.2 Limitations and Future Work 45

References 47

Appendix 1 – Adsorbent characterization 51

Appendix 2 – Waters' SFC-Unit 53

Appendix 3 – UV/VIS spectrums 54

Appendix 4 – Correlations for internal, external and global mass transfer coefficient 55

Appendix 5 – SF-TMB internal concentration profiles 57

Notation and Glossary

A	Area	(m^2)
C^o	Concentration that would exist in the reactor if the number of moles of the tracer were instantaneously and uniformly distributed in the reactor volume	(mol m^{-3})
C (t)	Danckwerts C curve	(mol m^{-3})
$C_{b,i}$	Bulk concentration of component i	(mol m^{-3})
$C_{p,i}$	Particle concentration in component i	(mol m^{-3})
$\overline{C_{p,i}}$	Average particle concentration in component i	(mol m^{-3})
C_T	Total bulk concentration	(mol m^{-3})
D_{12}	Molecular diffusion coefficient of infinite diluted solute (1) in solvent (2)	(m^2 s^{-1})
D	Column diameter	(m)
D_{ax}	Axial dispersion coefficient $\left(D_{ax} = \frac{u\,L}{Pe_p}\right)$	(m^2 s^{-1})
D_{ef}	Effective particle diffusion coefficient	(m^2 s^{-1})
d_p	Particle diameter	(m)
E(t)	Residence time distribution	(s^{-1})
$K_{ads,i}$	Adsorption equilibrium constant or Langmuir constant of component i	(m^3 mol^{-1})
k_L	Overall mass transfer coefficient (LDF)	(m s^{-1})
k_{ext}	External mass transfer coefficient	(m s^{-1})
k_{int}	Internal mass transfer coefficient	(m s^{-1})
M	Molar weight	(g mol^{-1})
n	Number of moles	(mol)
L	Column length	(m)
P	Pressure	(bar)
P_c	Critical pressure	(bar)
Pe	Péclet dimensionless number	(-)
Pe_p	Particle Péclet dimensionless number	(-)
Q	Volumetric flow rate	(m^3 s^{-1})
q_i	Average adsorbed phase concentration of component i	(mol m^{-3})
$Q_{sat,i}$	Maximum adsorption capacity of the adsorbent for component i	(mol m^{-3})
Re	Reynolds dimensionless number $\left(Re = \frac{u0\,d_p\,\rho}{\mu}\right)$	(-)
r_p	Adsorbent particle radius	(m)
Sc	Schmidt dimensionless number $\left(Sc = \frac{\mu}{\rho\,D_{12}}\right)$	(-)
Sh	Sherwood dimensionless number $\left(Sh = \frac{k_{ext}\,d_p}{D_{12}}\right)$	(-)
St	Stanton dimensionless number $\left(St = \frac{k_{ext}}{u0}\right)$	(-)
t	Time	(s)
T	Absolute temperature	(K)
T_c	Critical temperature	(K)

$\bar{t}_r$	Average residence time	(s)
u_0	Superficial fluid velocity	(m s^{-1})
u	Interstitial fluid velocity	(m s^{-1})
u_s	Solid interstitial velocity (TMB)	(m s^{-1})
V	Volume	(m^3) or (µl)
V_{int}	Interstitial column volume	(m^3)
V_m	Solute molar volume at normal boiling point	(cm^3 mol^{-1})
w%	Mass fraction	(%)
x	Column axial position	(m)
y_i	Molar fraction of total bulk concentration	(-)
z	Dimensionless column axial position $\left(z = \frac{x}{L}\right)$	(-)

Greek Letters

α	Particle macropore fraction (referred to area)	(-)
β	Safety coefficient	(-)
ε_b	Bulk porosity	(-)
ε_p	Particle porosity	(-)
γ	Fluid to solid flow rate ratio	(-)
λ_{max}	Maximum absorption wavelength	(nm)
µ	Solvent (CO_2) viscosity	(Pa)
μ_c	Critical viscosity	(Pa)
μ_r	Reduced viscosity $\left(\mu_r = \frac{\mu}{\mu_c}\right)$	(-)
ρ	Solvent (CO_2) density	(kg m^{-3})
ρ_c	Solvent (CO_2) critical density	(kg m^{-3})
ρ_r	Reduced viscosity $\left(\rho_r = \frac{\rho}{\rho_c}\right)$	(-)
τ	Column space time	(s) or (min)
τ_p	Particle tortuosity	(-)

Indexes

*	Equilibrium
—	Average
ads	Adsorbent
i	Compound
j	SMB column

List of Acronyms

ABPR	Automated Back Pressure Regulator	
Abs	Absorbance	(mUA)
DC_R	Desorbent Consumption (referring to the raffinate)	$L_{dessorbent}$ $kg^{-1}{}_{product}$
E	Eluent stream	
F	Feed stream	

HPLC	High Performance Liquid Chromatography	
LDF	Linear Driving Force model	
LLE	Liquid Liquid Equilibrium	
NRTL	Non Random Two Liquid (model)	
PUR_R	Raffinate Purity	
PUR_X	Extract Purity	
PR_R	Raffinate Productivity	$Kg_{product}$ L^{-1}_{ads} day^{-1}
R	Raffinate stream	
$ScCO_2$	Supercritical Carbon Dioxide	
SEM	Scanning Electron Microscopy	
SFC	Supercritical Fluid Chromatography	
SFC-FB	Supercritical Fluid Chromatography - Fixed Bed column	
SF-SMB	Supercritical Fluid Simulated Moving Bed	
SF-TMB	Supercritical Fluid True Moving Bed	
SMB(R)	Simulated Moving Bed (Reactor)	
TMB	True Moving Bed	
X	Extract stream	

List of Figures

Figure 1 – Scheme of the reaction between glycerol and acetone in acid media to produce solketal. Reprinted from reference [6]. 4

Figure 2 – left) – acetone-solketal-glycerol experimental LLE data and binodal curve using the NRTL model at 323.2 K and 1.013 bar: (■) experimental tie-lines; (--) NRTL bimodal curve, adapted from reference [17]; right) glycerol(1)- water(2)- acetone (3) experimental LLE data at 298.15 K, adapted from reference [18, 19]. 7

Figure 3 – pressure versus CO2 mole fraction diagram for the ScCO2/glycerol system: glycerol-rich phase (left) and CO2-rich phase (right). Adapted from reference [20]. 7

Figure 4 - Phase equilibrium behavior for the system water (1) - acetone (2) - CO2 (3) at 333 K and from the top left to the right bottom: 27.6, 40, 60, 80, 100 and 150 bar: experimental phase compositions (•) and tie-lines (—) ; predicted tie-lines (—) ;predicted three-phase equilibrium compositions (Δ). Adapted from reference [22] 8

Figure 5 - Pressure-composition diagram for the systems CO_2 (1) + solketal (2) at T = 308 K (circles) and T = 338 K (squares). Adapted from reference [23] 9

Figure 6 – Scheme of the Waters® SFC experimental set-up. Adapted from reference [11]..... 14

Figure 7 - Scheme of a TMB and the desired fluxes of each species to guarantee the complete separation. [40] 18

Figure 8 – Average injected amount for each compound for all loops and operating conditions. Only validated data is represented on each average point, the outsider points were not considered. 26

Figure 9 - Experimental C(t) data and correspondent adjusted curve with SFC-FB gPROMS' model for **acetone**. From the top to the bottom: at 150 bar/313 K; 150 bar/353 K; 200 bar/313 K. The estimated kL, $Kads$ and $Qsat$ parameters resulting from this fit are summarized in Table 10. .. 31

Figure 10 - Experimental C(t) data and correspondent adjusted curve with SFC-FB gPROMS' model for **solketal.** From the top to the bottom: at 150 bar/313 K; 150 bar/353 K; 200 bar/313 K. The estimated kL, $Kads$ and $Qsat$ parameters resulting from this fit are summarized in Table 11. .. 32

Figure 11 – Experimental C(t) data and correspondent adjusted curve with SFC-FB gPROMS' model for **water.** From the top to the bottom: at 150 bar/313 K; 150 bar/353 K; 200 bar/313 K. The kL, $Kads$ and $Qsat$ parameters resulting from this fit are summarized in Table 12. 33

Figure 12 - Acetone Langmuir adsorption isotherm at the studied concentrations at the tree operating conditions simulated, using the Langmuir constants liquid e Q_{sat} found on Table 10. 35

Figure 13 - Solketal Langmuir adsorption isotherm at the studied concentrations at the tree operating conditions simulated, using the Langmuir constants K_{ads} e Q_{sat} found on Table 11. 35

Figure 14 – Water Langmuir adsorption isotherm at the studied concentrations at the tree operating conditions simulated, using the Langmuir constants K_{ads} e Q_{sat} found on Table 12. 36

Figure 15 – Comparison of the water and solketal Langmuir adsorption isotherms at 150 bar and 313 K: water noncompetitive (NC); water competitive (C); water dual site competitive (DSC); solketal noncompetitive (NC); solketal competitive (C); α = 0.412. $Kads$ and $Qsat$ parameters can be found on Table 11 and Table 12. 38

Figure 16 - Separation regions for the three scenarios at the reference operating conditions 150 bar /313 K. 40

Figure 17 - Separation regions for the three water Langmuir adsorption models at the operating conditions 200 bar /313 K. 40

Figure 18 – Separation regions for the three water Langmuir adsorption models at the operating conditions 150 bar /353 K. 41

Figure 19 – Acetone UV/VIS absorption spectrum. Reprinted from [47]. 54

Figure 20 – Solketal UV/VIS absorption spectrum. Reprinted from [48]. 54

Figure 21 – Water UV/VIS absorption spectrum. Reprinted from [49]. 54

List of Tables

Table 1 – Compounds physical properties of interest to this work [8, 34]. (a) the values refer to the minimum and maximum projection diameter, obtained with a software tool (Chemicalize ©). . 11

Table 2 – Zeolite HBEA-25 relevant properties for this work. 12

Table 3 – SFC-FB parameters. 14

Table 4 – Experimental SFC-fixed bed column conditions. The variables are the compound analyzed, the loop injection volume and the operating pressure and temperature. 15

Table 5 - Density (kg m^{-3}) of pure $ScCO_2$ at the working conditions [15]. 23

Table 6 - Correlations for estimation of the axial dispersion in a fixed bed column. 24

Table 7 – Summary of tr (min) for solketal pulse injections (runs of 45 min) in different operating conditions – loop volume (µl) versus temperature (K) and pressure (bar). 27

Table 8 – Summary of tr (min) for acetone pulse injections (runs of 25 min) at different operating conditions – loop volume (µl), temperature (K) and pressure (bar). 28

Table 9 – Summary of tr (min) for water pulse injections (runs of 90 min) in different operating conditions – loop volume (µl) versus temperature (K) and pressure (bar). 28

Table 10 – Estimated kL (m s^{-1}), $Kads$ (m^3 mol^{-1}) and $Qsat$ (mol $m_{sol.}^{-3}$) for **acetone** (runs 4 to 9 and 13 to 15)**; solketal** (runs 19 to 24 and 28 to 30) **and water** (runs 31 to 40) at **150 bar/313 K**, **200 bar/313 K** and **150 bar/353 K**, using all concentrations pulses. 34

Table 13 - Operating parameters for the TMB. 39

Table 14 - Performance parameters for the SF-TMB at three different operating conditions (150 bar /313 K; 200 bar /313 K; 150 bar /353 K), considering the three Langmuir adsorption isotherm model hypothesis. 41

1 Introduction

1.1 Motivation and relevance

The worldwide search for alternatives to fossil fuels depletion and economic independence boost the search for new green renewable energy and its increasing production, with biodiesel as one of the most important. Biodiesel production has increased remarkably in this century, along with its reaction byproduct, the glycerol. This crude glycerol has almost no value and its valorization became a priority to improve biodiesel industry economic and environmental competitiveness.

A lot of solutions have been proposed for crude glycerol valorization. One of them is the production of a green fuel additive, the solketal, by the reaction between glycerol and acetone, a reaction with almost 100% selectivity, unlike other glycerol reactions. Solketal is considered a safe compound and has innumerous applications, yet the most promising is as a green fuel additive, which can be blended with biodiesel itself to improve its octane number and stability.

Although a lot of research in homogeneous and heterogeneous reaction catalysts has been done, problems concerning process scale up still persist. Glycerol high viscosity and acetone very low solubility in glycerol at normal conditions are reaction obstacles that need to be overcome to turn solketal into an economic and sustainable glycerol valorization solution. Some integrated processes like reactive distillation have already been proposed, but yet no industrial scale process is found.

The solution proposed and investigated in this work relies on operating in supercritical conditions as a solution to improve system mass transfer issues and provide an efficient and environmental friendly solketal separation process. Supercritical carbon dioxide appears to be an excellent option for solketal production reaction and separation due to its properties and as the most used supercritical fluid in industrial processes. It is a nontoxic, nonflammable solvent and it is nonreactive with the system compounds. Along with its readily attainable critical point of 74 bar and 304 K, one of the major advantages of supercritical carbon dioxide is its easy separation from the compounds, just by depressurizing the system below the critical point and the possibility to recycle it with no further processes.

The objective of this thesis is to simulate and design in gPROMS' software a supercritical TMB to separate solketal from water, using a high water affinity HBEA-25 zeolite as adsorbent. The data to simulate the TMB was obtained experimentally by running and mathematically modeling water, solketal and acetone pulse experiences in a supercritical chromatographic fixed bed column with carbon dioxide as eluent, under different operating conditions.

1.2 Thesis outline

First, in **Chapter 2** is summarized the actual crude glycerol increasing production as a biodiesel byproduct with almost no economic value. The state of the art of the reaction with acetone to produce solketal, a high value product, along with water and solketal separation from water is presented. To overcome some reaction and separation problems, like high viscosities, mass transfer problems and low glycerol solubility in acetone, a process using $ScCO_2$ as solvent is proposed. Supercritical fluids properties are analyzed as well as their influence on system phase equilibrium at high pressure (when available), which is essential to design supercritical processes. To finish, some of the very few solketal separation processes available in literature are presented and laboratorial/pilot scale supercritical separation processes are presented.

In **Chapter 3,** a characterization of the materials used is made, especially of the reagents and the adsorbent zeolite HBEA-25. The experimental unit to operate at high pressures is described as well as the experimental pulse procedure for acetone, solketal and water at different concentrations, temperatures and pressures. The mathematical model to describe the SFC-fixed bed column pulse experiences and the model to simulate and design a SF-TMB are also presented in detail. To finish, values of $ScCO_2$ viscosity and density at the operating conditions of interest, an equation to estimate solute molecular diffusivities in supercritical carbon dioxide and different correlations to estimate the fixed bed Péclet number are presented.

In **Chapter 4**, the results of the pulse experiments are presented as well as its mathematical modeling in gPROMS to estimate the parameters k_L, K_{ads} and Q_{sat}. The equilibrium adsorption isotherms are fitted to a Langmuir model. In **section 4.4**, a supercritical TMB is designed and its performance studied for different operating conditions.

Finally, in **Chapter 5** the major conclusions of this work are summarized and some future work and improvements that need to be done to better describe and support supercritical separation processes, especially solketal separation, are presented.

In the **Appendix** section, complementary data and information may be found to better understand this work.

2 Context and State of the art

The fossil fuel depletion and economic dependence of the market and companies on fossil fuels companies, together with the environmental impact and degradation associated to their exploration and use, created a new reality for renewable energy sources that opened the global scientific and market community interests on renewable energy sources

The biodiesel is considered as an attractive alternative to diesel fuels, because it is renewable, biodegradable, nontoxic and has almost the same properties as diesel fuel. Traditionally used in road transports, biodiesel gained since 2006 a larger scale usage in aviation, to generate electricity, for cooking and even in maritime transport. In 2013, the global biodiesel production reached more than 110 thousand million liters. Biodiesel is mainly produced by the transesterification of vegetable oils or animal fat (triglyceride) with a mono-alcohol, usually methanol or ethanol, using homogeneous catalysed basic conditions. It can be used directly or after blending with fossil-based diesel fuel [1-3].

Biodiesel consumption in the European Union increased 78.5% between 2007 and 2012, reaching 13.8 million liters in 2012. It is expected to reach 41 billion liters by 2022, with the expanded Renewable Fuel Standard in the United States of America (USA), along with EU-RED, contributing to the continued global biofuels market expansion [4].

In the biodiesel industry, during the transesterification process, about 10 w% of the reaction products is crude glycerol, the main byproduct, which contains impurities such as water, inorganic salts, methanol, fatty acids, esters, etc., resulting in a glycerol content from 40 to 88%, depending on the type of oil and process used, a purity level far below the technical (88-98%) and pharmaceutical (>98%) quality, resulting in a product with almost no economic value [1, 3, 5]. So, along with the increasing biodiesel production, an excessive amount of glycerol is expected to accumulate, leading to a decrease on the crude glycerol economical value, which has lowered from 0.47 €/kg in 2004 to 0.15 €/kg in 2011 [1, 3].

Glycerol cannot be added directly to fuels due to its decomposition and polymerization which would lead to engine problems at high temperature. In the past, crude glycerol was therefore commonly treated as a waste stream of biodiesel industry and it was incinerated for energy recovery. With its lower price and the need of more green processes, it is important to convert glycerol into added-value products, enhancing biodiesel competitive and sustainable value. Some of the options are even fuel additives [1, 3, 6]. The conversion of low value crude glycerol to produce value-added chemicals such as propanediols, acrolein, dihydroxyacetone, glyceric acid, tartonic acid, epichlorohydrin, hydrogen, syngas, ethers, esters, etc., has a tremendous potential to make glycerol a valuable chemical platform.

2.1 Solketal: a product of glycerol and acetone reaction

One of the best options is the production of cyclic acetals and ketals, reacting glycerol with aldehydes and ketones, respectively. It is believed to be one of the most promising glycerol applications as fuel/chemical intermediates, modifying them to derivatives which are excellent compounds for gasoline, diesel and biodiesel blends. They improve the octane number, the oxidation stability, the cold flow properties of liquid transportation fuels, reduce particulate emission and gum formation in diesel and biodiesel fuels. One of these cyclic acetals is the 2,2-dimethyl-1,3-dioxolane-4-methanol (solketal) produced by the ketalization reaction between glycerol and acetone over an acid catalyst. The reaction is described by the scheme in Figure 1 [1, 3, 6].

Solketal is considered a safe compound, classified as a non-toxic species and incorporated in the so-called bio-based solvents, a class of commodity chemicals that already represent a mature market. It has been widely used as a versatile solvent in several large-scale applications like in paint and ink formulations, cleaning products, as a cooling agent, as plasticizer in the polymer industry and as a solubilizing and suspending agent in pharmaceutical preparations. [3, 7].

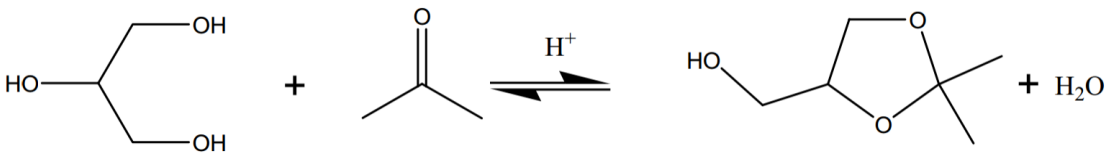

Figure 1 – Scheme of the reaction between glycerol and acetone in acid media to produce solketal. Reprinted from reference [6].

The reaction to produce solketal can be described by the general reaction to prepare glycerol acetal/ketal. Acetal/ketal formation is a reversible reaction via a two-step mechanism: the first is the formation of a hemiacetal (considered the rate determining step) followed by the its dehydration. Cyclic acetals/ketals are prepared by reacting a polyol with the appropriate aldehydes or ketones. When glycerol is used as polyol, the 1,3 dioxane and 1,3 dioxolane structures are formed. Cyclic ketals, specifically solketal, formed by the reaction of glycerol and ketones, have a 1,3 dioxolane structure (5 membered ring) instead of a 1,3 dioxane (6 membered ring) due to the steric blocking of radicals and hydrogen atoms from positions 4 and 6 of the molecule. This explains why the reaction between glycerol and acetone usually has almost 100% solketal selectivity, making the reaction very attractive due to the very low formation of byproducts [1].

Acetalization/ketalization of glycerol is highly dependent on the experimental conditions, requiring a production process optimization [1]. Glycerol is poorly miscible with acetone at standard ambient conditions (298K and 1 atm), with only 5 wt% of glycerol soluble in acetone, and the solubility does not improve significantly with higher temperatures and pressures, becoming a major disadvantage for the synthesis of solketal. Also, glycerol high viscosity hampers the reaction, leading to major mass transfer problems, especially in continuous flow processes. Pure glycerol viscosity is 749.34 and 37.5 mPa at 298.15 K and 353.15 K respectively, being much more viscous that all the other components involved in the reaction. [1, 8]. However, crude glycerol average viscosity is much lower due to the presence of impurities, 8.5 mPa at 313.15 K, facilitating the processes.

2.2 Supercritical fluids

Motivated by the need to improve the reaction kinetics, particularly, the mass transfer issues, using supercritical fluids as solvent and or eluent comes as an option to be explored. Briefly, supercritical fluids' laboratorial and industrial interest relies on its unique features such as liquid-like densities and solvent power, gas-like viscosities, intermediate typical gas and liquid diffusivities and the ability to drastically change its properties (like solvent power) only with small changes in temperature and/or pressure, specially near its critical point. [9-11]

Solketal production in supercritical conditions was already proposed by Royon et al [6]. They proposed the synthesis of solketal without using any catalyst, considering that the reactant supercritical acetone also acts as catalyst when supercritical conditions are achieved (508K and 47 bar), due to the acidic property of the alpha hydrogen of the acetone. It also improves glycerol solubility in acetone, mass transfer coefficients and reduce solution viscosity. However, since ketalization is an exothermic process, high temperatures are thermodynamically unfavorable to solketal formation. Also, supercritical acetone catalyzes glycerol conversion to acrolein and its further polymerization due to the high pressure and temperature operating conditions. So even optimizing the operating conditions to a somewhat ideal situation of 80 bar, 523K and very diluted solution (high acetone/glycerol molar ratio of 10.8), it took 4h to achieve a very low 28.2% glycerol conversion and a solketal selectivity of 80%, a result with no industrial interest. Also the high temperature operating costs reduces the industrial interest. [1, 3, 6, 12] Even so, this reaction approach could be an interesting option if an appropriate catalyst is used, because no additional solvent is used, making the solketal purification easier and taking advantage of the supercritical properties.

Inspired by this previous work, supercritical carbon dioxide ($ScCO_2$) appears to be an excellent option to solketal production reaction and/or separation due to its properties and

well established industrial supercritical processes. Biodiesel production or caffeine extraction are examples of industrial processes using $ScCO_2$ [11].

Carbon dioxide (CO_2) is considered the most important solvent in supercritical conditions. Besides of its nontoxic and nonflammable properties, it has a readily attainable critical point, with a moderate 73.72 bar critical pressure and a critical temperate slightly above the ambient temperature, an attractive 304.11 K [13]. CO_2 usually comes either as a chemical industry byproduct or from natural processes like beverage fermentation and so it should not increase the greenhouse effect. The low critical point together with the commercial availability at moderate cost and reduced environmental impact turns $ScCO_2$ into a cheap and ecological supercritical fluid. [10, 11, 14]. $ScCO_2$ does not react with the reagents and products of the studied reactive system, it has a great dissolution power for many compounds and enhanced transference properties (low viscosity and high diffusion coefficient) which is the critical step in several processes. These properties are controlled by its density, adjusting the system pressure and temperature [10].

The productivity of the operational unit is typically limited by the feed solubility in the mobile phase. The pure $ScCO_2$ dissolution power could not be enough for some polar compounds, fact that can be overcome by adding organic co-solvents to tune $ScCO_2$ polarity and properties. That procedure would lead to the loss of the “organic solvents free” process label and to the increase of the complexity of the product purification step. However, the raw material, crude glycerol, actually has polar impurities such as methanol in its constitution, which can automatically tune the $ScCO_2$. The reagent acetone is itself a traditional co-solvent to tune $ScCO_2$ polarity and increase its dissolution power [15, 16]. These situations probably remove the need to add external co-solvents to the system [10, 11]. Another big advantage of $ScCO_2$ is the easy separation from the products and unreacted reagents by just depressurizing the system, allowing $ScCO_2$ recycling and reducing or even eliminating the need to remove other solvents that may be added to the reactional/separation system [10] .

2.3 Equilibrium data

There is no equilibrium data for the reactive system with $ScCO_2$ as solvent. It was not possible to evaluate the phase equilibrium of the system in this work due to the lack of equipment available for that purpose. So, to have an idea on the system behavior, some equilibrium data is presented to be aware of the reactants and products solubility in pure $ScCO_2$ and the equilibrium established between phases.

In Figure 2 (left) it is presented the system liquid-liquid equilibria (LLE) by a ternary phase diagram for the two reagents and the product of interest. Solketal is totally soluble in both reactants, but the reagents themselves are poorly miscible in each other. Nevertheless, at

323.2 K, if the solketal molar fraction (x_{sk}) remains above 0.159, the reagents become totally soluble and there is only one phase [17]. Analyzing Figure 2 (right), it is visible that both glycerol and acetone are, each one, totally soluble in water. Yet, the system glycerol water acetone is also biphasic because, as discussed above, acetone is poorly miscible in glycerol [18, 19].

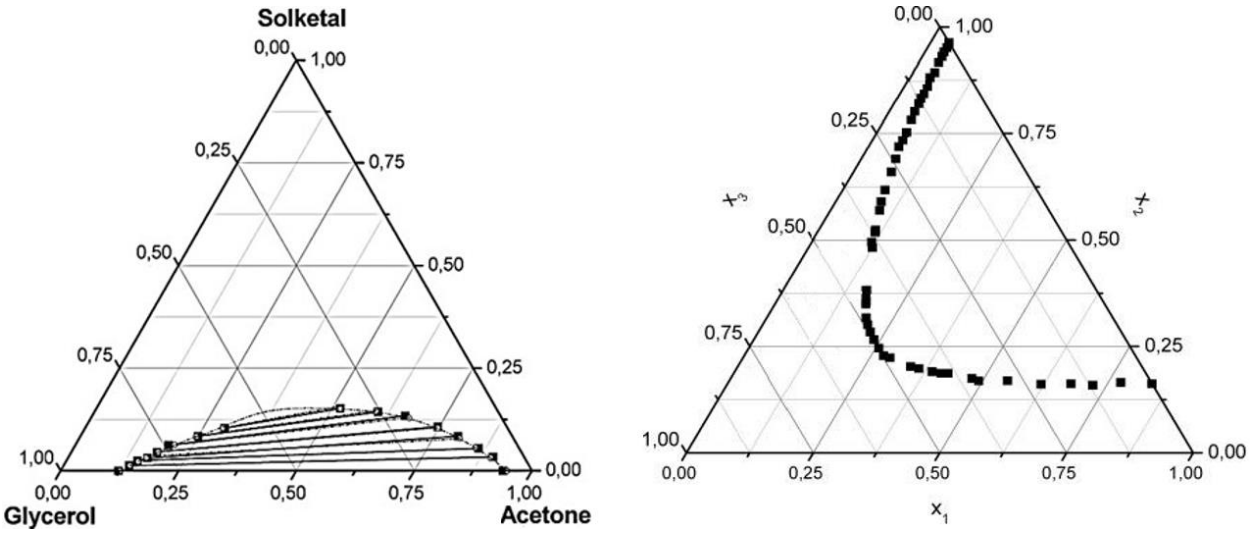

Figure 2 – (left) – acetone-solketal-glycerol experimental LLE data and binodal curve using the NRTL model at 323.2 K and 1.013 bar: (■) experimental tie-lines; (--) NRTL bimodal curve, adapted from reference [17]; (right) - glycerol(1)- water(2)- acetone (3) experimental LLE data at 298.15 K, adapted from reference [18, 19].

It is now important to analyze the equilibria of the chemical compounds in the presence of $ScCO_2$. Regarding the $ScCO_2$/glycerol system, it is always biphasic for temperatures ranging from 313 to 473 K and pressures up to 350 bar. Concerning the CO_2 rich phase, the glycerol solubility in CO_2 is extremely low, in the range of 0.10 to 0.05 mole fraction, while the glycerol rich phase can dissolve CO_2 up to 0.1 mole fraction. A better perception of the behavior can be observed in Figure 3 [20].

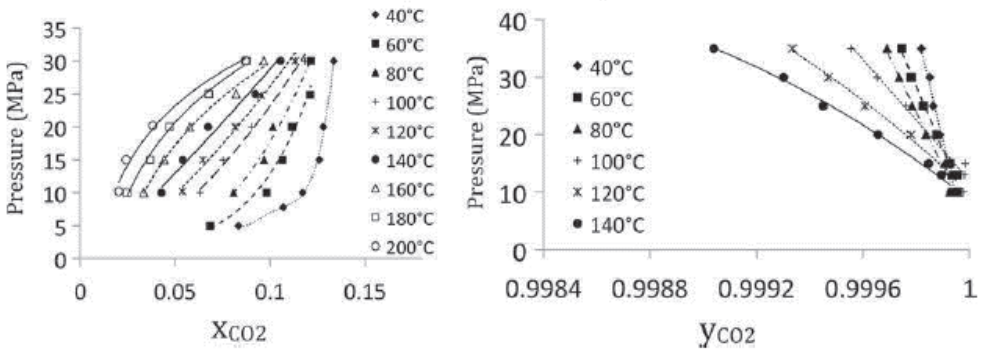

Figure 3 – pressure versus CO2 mole fraction diagram for the ScCO2/glycerol system: glycerol-rich phase (left) and CO2-rich phase (right). Adapted from reference [20].

Data is also available for the ternary phase system equilibrium between water, acetone and CO_2 in subcritical and supercritical state at 333 K and a range of pressures from 20 to 150 bar,

represented in Figure 4. It is interesting to observe that the complex phase diagram observed at subcritical conditions, with acetone being poorly miscible in subcritical CO_2, becomes much simpler in supercritical state with acetone becoming totally soluble in S_CCO_2. Acetone solubility together with its polarity makes it a good co-solvent to tune S_CCO_2 polarity and dissolution power [15, 16]. Water is practically immiscible in CO_2 for sub and supercritical state (at the conditions analyzed) [15, 21, 22].

Solketal, on the other hand, has an excellent solubility in CO_2. For this binary system, VLE data is available at different compositions, some of which are plotted in Figure 5. Notice that the data at 338 K is for pressures above 74 bar, so the CO_2 is in supercritical phase [23].

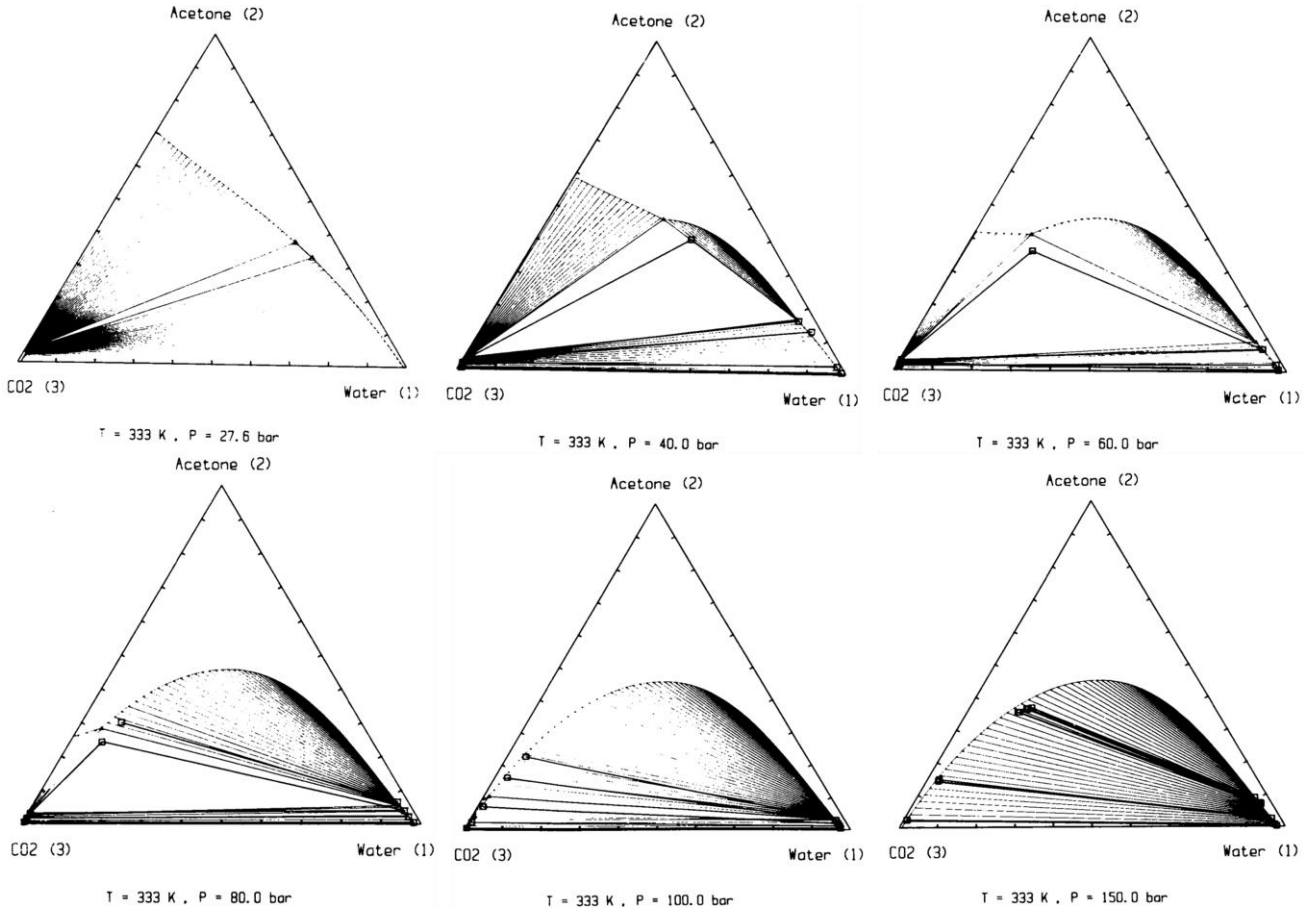

Figure 4 - Phase equilibrium behavior for the system water (1) - acetone (2) - CO2 (3) at 333 K and from the top left to the right bottom: 27.6, 40, 60, 80, 100 and 150 bar: experimental phase compositions (•) and tie-lines (—) ; predicted tie-lines (—) ;predicted three-phase equilibrium compositions (Δ). Adapted from reference [22].

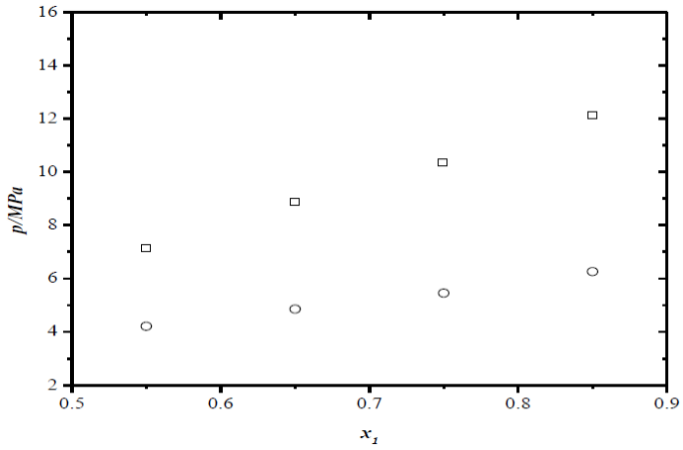

Figure 5 - Pressure-composition diagram for the systems CO_2 (1) + solketal (2) at T = 308 K (circles) and T = 338 K (squares). Adapted from reference [23].

2.1 Supercritical separation

In this work, it is explored the separation of solketal from the remaining byproduct, water. Typically, glycerol is the limiting reactant and acetone is present in large excess, resulting in an ideal reactive mixture without glycerol. A separation study with acetone and some glycerol residues could be done, but it will not be viable for this study due to time and resources available.

It was found almost no work about the separation of solketal. Some articles refer to simple distillation just for laboratorial analysis purpose [24]. Clarkson et al. (2001) [25] propose a continuous counter-current reactive distillation with numerous plates to remove water and drive the equilibrium to the formation of solketal, obtaining purified solketal as tale product. This is a good solution because the reaction and separation are on the same unity, and the heterogeneous catalyst is recycled, but for scale up some problems have been found such as high energy consumption (traditional in distillation processes), the need to separate unreacted acetone from water for reagent recycling, high residence time and the formation of byproducts due to the high temperatures. The process can achieve 15kg of solketal/hr for a 0.15 m column [25].

First generation of industrial SMB separation processes started being commercialized in the 1960s by the UOP Inc for petrochemical and sugar industry. The second generation of SMB comes in the 1990s applied to fine chemical separation (pharmaceutical and biomolecule separations). [26]. Compounds similar to solketal such as acetals were successfully produced and separated using the simulated moving-bed reactor (SMBR) technology based on modeling and simulation studies and laboratorial and pilot scale experiments: acetaldehyde diethylacetal [27], diethylacetal [28, 29], 1,1-dibutoxyethane [30, 31], 1,1-diethoxyethane [31], 1,1-dimethoxyethane [31].

One of the innovations proposed in this work is the use of $ScCO_2$ as the mobile phase in the SMB technology to purify solketal. This is not a misplaced solution, actually the use of $ScCO_2$ as eluent in a chromatographic column and the development of a supercritical fluid chromatography (SFC) equipment was first proposed by Klesper in the 60's. The commercial development of preparative SFC started in the 1980's.

The use of SFC has some advantages compared to the classical HPLC. It is often said that SFC is 3 to 5 times faster. Low fluid viscosity and increased diffusivity leads to shorter retention times and increased productivity because the mobile phase velocity can be significantly higher. It also allows the use of longer columns packed with small particles with lower pressure drop leading to higher linear velocities. Also, under supercritical conditions, the chromatographic column is equilibrated in a few minutes instead of hours like in classical HPLC. Due to these reasons, there has been a lot of progress in packed columns for supercritical fluid chromatography [10, 32].

The adaptation of a SFC to a continuous chromatography process, a true moving bed (TMB) or to a simulated moving bed (SMB), is possible. The SF-SMB has a lot of advantages compared to liquid elution chromatography and was first reported by Mazzotti et al. in 1997 [33].

The SF-SMB has the advantage of being able to modify the elution strength in different zones via pressure and temperature modification, unlike the traditional liquid chromatography based SMB, an isocratic process. As so, the SF-SMB leads to new options of advanced separation. Improvements in productivity when the SF-SMB unit is operated in pressure gradient vs. isocratic mode were reported by Mazzotti et al. in 1997 [33] and Miller in 2012 [32]. The well know triangle theory is also applied to SF-SMB [10, 32, 33].

Despite the progress, a SF-SMB has high equipment and operating costs. A typical SF-SMB unit contains four to five pumps, 6–12 columns and many high speed switching valves, all designed to operate under high pressure conditions.

The SF-SMB is already a laboratorial and pilot scale reality, for example tested for the separation of fatty acids ethyl esters, the purification of phytol, ibuprofen, bi-naphthol and 1-phenyl-1-propanol, the separation of bi-naphthol enantiomers, the chiral resolution of α-tetralol and the separation of trans-stilbene oxide (TSO) racemate [10, 32].

Some examples of developed SF-SMB equipment are a SFC Series SF3 Gilson System with a 4.6x250 mm analytical column packed; a continuous NOVASEP SFC unit with eight columns of 200 mm bed length and 0.33 mm internal diameter each and uniform or gradient pressure (for productivity improvement) operation mode. At pilot scale, a SF-SMB SUPERSEP 50 with a 50 mm internal diameter DAC column, a maximum 1 kg/min CO2 flow rate and 99% purity levels for enantiomers [10].

3 Materials and Methods

3.1 Materials

3.1.1 Chemicals

The compounds used in this work are acetone (99.5+%, CHEM_LAB®), solketal (97%, Acro Organics®) and deionized water obtained in LSRE laboratory. The eluent is CO_2 (99.998%, O_2 ≤ 2 ppm, CnHm ≤ 2 ppm, H2 ≤ 0.5 ppm, H_2O ≤ 3 ppm, Air Liquide® bottle equipped with a dip tube). The need of a pressurized bottle with siphon is to guarantee the supply of liquid CO_2 to the HPLC pump. Some physical properties of these compounds are given in Table 1.

Propan-2-ol (analytical reagent grade, Fisher Chemical®) was used as syringe cleaning solvent.

Table 1 – Compounds physical properties of interest to this work [8, 34]. (a) the values refer to the minimum and maximum projection diameter, obtained with the Chemicalize © software.

Properties	Acetone	Solketal	Water	CO_2
Freezing Point (K)	178.45	246.75	273.15	216.58
Boiling Point (K)	329.44	450.759	373.15	194.67
M (g mol^{-1})	58.08	132.16	18.02	44.01
ρ (Kg m^{-3}) at 298.15 K	786	1064 (at 293.15 K)	997	713
V_m at normal boiling point (mol cm^{-3})	77.638	124.210	18.798	35.019
T_c (K)	508.20	-	674.10	304.19
P_c (bar)	47.02	-	220.64	73.82
ρ_c (kg m^{-3})	277.9	-	321.91	468.2
Molecular critical diameter (Width) (Å)	3.08 [35]	6.96 to 9.48 (a)	1.93 [35]	2.80

3.1.2 Zeolite HBEA-25

For the separation experiments, the adsorbent chosen to pack the SFC-column was zeolite HBEA-25, a nano-porous BEA having a SiO_2/Al_2O_3 molar ratio of 25:75. The material is from Süd-chemie. This material can be employed as catalyst for the solketal production reaction and also as adsorbent. It has a very high affinity for water when compared to solketal, which makes it a good adsorbent for the separation of the two products of the ketalization reaction.

The zeolite HBEA-25 used was supplied in the form of pellets and was reshaped on a spheronizer and sieved to obtain a fraction with particle diameters between 0.600 and 1.180 mm and an approximated spherical geometry.

To ensure the zeolite quality, a comparison between the X-Ray diffraction results obtained for the HBEA-25 sample used in this study and the XRD standard pattern taken from the IZA database [36] was made (see Appendix 1). A match between the peaks positions is observed, concluding that the material is HBEA-25.

The macroporosity of the material was assessed by mercury porosimetry (pressure from 0.035 to 2275 bar and Hg contact angle of 130º) using an AutoPore IV 9500 by the IPN led&matm, Laboratório de Ensaios e Desgaste & Materiais, to determine the particle porosity and density. As Hg only penetrates in the macro and major mesoporous, the macro and meso particle porosity was determined. The estimated particle porosity (ε_p) was 0.326.

CO_2 adsorption equilibrium isotherm at 273.15 K were measured (see Appendix 1) and the results were analyzed by the Horvath-Kawazoe method. A micropore size distribution range from 4.0 to 6.5 Å, with a median pore width of 5.1 Å was determined. The N_2 adsorption equilibrium isotherm at 77K, (see Appendix 1), gives a micropore area of 265.8 $m^2\ g^{-1}$ and a macropore area of 186.2 $m^2\ g^{-1}$.

The main zeolite properties are summarized in Table 2. A Scanning Electron Microscopy (SEM) of the zeolite HBEA-25 may be found in Appendix 1.

Table 2 – Zeolite HBEA-25 relevant properties for this work.

Properties	Value
Chemical formula	SiO_2/Al_2O_3, molar ratio 25:75
Particle diameter (mm)	0.600 to 1.180
Apparent density (kg m^{-3})	1369
ε_p (assessed by Hg porosimetry)	0.326
Micropore size (Å) (CO_2 adsorption isotherm at 273.15K)	5.1
Micropore area (m^2/g) (N_2 adsorption isotherm at 77K)	265.8
Macropore area (m^2/g) (N_2 adsorption isotherm at 77K)	186.2

3.2 Experimental set-up

3.2.1 SFC-unit

A supercritical fluid chromatograph (SFC) from Thar®/Waters®, represented schematically in Figure 6, was used to carry out the experiments, together with Waters® software. The photograph of the equipment can be seen in Appendix 2. The modular installation is composed by:

The **fluid delivery module**, which has a CO_2 delivery pump with three peristaltic head pumps and flow capacity range from 0.1 to 10 ± 0.1 mL min^{-1}. The liquid CO_2, stored on a dip tube bottle at about 60 bar and room temperature, is pumped into the system. The delivery pump is continuously cooled down by an external heat exchanger set at 276 K, guaranteeing that the CO_2 is in liquid state and able to be pumped. There is also a cosolvent delivery pump with two peristaltic head pumps and a flow capacity range from 0.01 to 10 ± 0.01 mL·min^{-1}. The co-solvent fraction may vary from 0 to 100%.

The **auto sampler module**, which has two plates of 48 vials each and a syringe-loop module. The injection loop volume is adjustable by changing the loops, in this work the available volumes are 10, 50, 100 and 200 µL. The full loop injection mode is used, pushing the double of the desired injection volume to assure that the loop is cleaned and completely filled, rejecting the first sample volume. The automatic syringe cleaning system uses propan-2-ol as a cleaning solvent.

The **column oven**, where the SFC columns are horizontally disposed, up to 10 columns simultaneously. The temperature is controlled automatically, ranging from 273 to 353 K, with a resolution of 0.1 K. It is where the by-pass tube and the fixed bed column filled with zeolite HBEA-25 are disposed.

The **UV spectrophotometer**, which consists on a deuterium lamp in continuous flux cell with a wavelength range from 190 to 800 nm with a 1.2 nm maximum resolution and a maximum 400 bar operating pressure. The software plot a complete 3D absorbance versus time graph, giving an excellent image of all the dynamic UV spectrum. It is possible to obtain 2D plots at up to 8 different wavelength values.

An **automated back pressure regulator (ABPR)**, used to maintain the desired pressure inside the column, it can operate in the range from 5 to 400 bar, with a 3 bar minimum pressure drop. It has an auxiliary heat exchanger to maintain the temperature at 308 K, in order to prevent possible freezing of the solution in the valve due to the temperature drop caused by CO_2 depressurization.

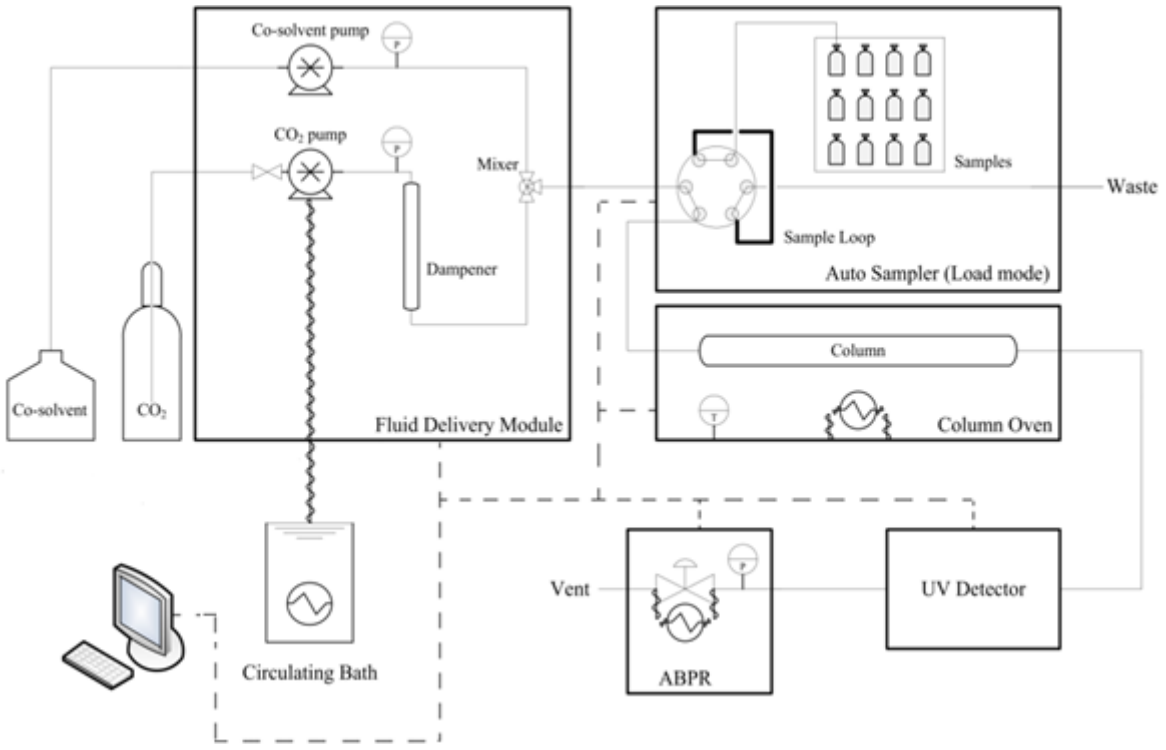

Figure 6 – Scheme of the Waters® SFC experimental set-up. Adapted from reference [11].

3.2.2 SFC-fixed bed column

A column with 0.4 cm internal diameter and 12.5 cm of length is packed with zeolite HBEA-25 with 0.1 cm average diameter. To properly estimate the supercritical fixed bed chromatography column (SFC-FB) bed voidage (ε_b), the Dixon correlation designed for fixed beds [37] is used, defined by equation (1). For the correspondent $\frac{d_p}{D}$ of 0.25, the Dixon correlation gives a ε_b of 0.438. The eluent volumetric flow is kept constant at a value of 2 ml min^{-1} so, by equation (2) the column space time is 0.415 min. This properties values are summarized in Table 3.

Table 3 – SFC-FB parameters.

Property	Value
Q_{CO_2} (cm^3 min^{-1})	2.00
$d_{p,average}$ (cm)	0.1
ε_b	0.438
D (cm)	0.4
L (cm)	12.5
V_{int} (cm^3)	0.831
τ (min)	0.415

$$\varepsilon_b = 0.4 + 0.05\,\frac{d_p}{D} + 0.412\left(\frac{d_p}{D}\right)^2 \qquad \left(\frac{d_p}{D} > 2\right) \qquad (1)$$

$$\tau = \frac{Vint}{Q_{CO_2}}\,(min) \qquad (2)$$

3.3 Experimental procedure (pulse experiments)

To obtain experimental adsorption data about the system in study and fit it into the SFC-fixed bed column model and simulate a SF-TMB, a series of experimental injection in the SFC-fixed bed column were made.

The data is measured by an UV flux cell with a photodiode array detector, obtaining the dynamic absorbance signal response with time. The acquisition UV wavelength is 196, 220 and 230 nm for water, solketal and acetone respectively. The acquisition wavelength choice is explained later in the results and discussion chapter.

The experimental pulse injections are summarized in the Table 4. The variables changed on the system were the injected compound (acetone, solketal, water), the injection volume (10, 50, 100 and 200 µL), the operating temperature (313.15, 333.15 and 353.15 K) and the operating pressure (100, 150 and 200 bar). All the runs have at least three reproducible injections, up to 12 repetitions for same cases, like 100 bar injections and water pulses.

Table 4 – Experimental SFC-fixed bed column conditions. The variables are the compound analyzed, the loop injection volume and the operating pressure and temperature.

Run	Compound	Loop injection volume (µl)	Pressure (bar)	Temperature (K)
1/2/3	Acetone	50/100/200	100	313
4/5/6	Acetone	50/100/200	150	313
7/8/9	Acetone	50/100/200	200	313
10/11/12	Acetone	50/100/200	150	333
13/14/15	Acetone	50/100/200	150	353
16/17/18	Solketal	50/100/200	100	313
19/20/21	Solketal	50/100/200	150	313
22/23/24	Solketal	50/100/200	200	313
25/26/27	Solketal	50/100/200	150	333
28/29/30	Solketal	50/100/200	150	353
31/32/33/34	Water	10/50/100/200	150	313
35/36/37	Water	10/50/100	200	313
38/39/40	Water	10/50/100	150	353

All the obtained pulse injections are analyzed visually and, using the residence time distribution theory, converted into the correspondent E(t) and C(t) curve using equations (3) and (4) respectively. From equation (5) it is calculated the $C^o\tau$ (mol min m^{-3}) for equation (4). The average retention time $\bar{t}_r$ is obtained from equation (6).

$$E(t) = \frac{Abs(t)}{\int_0^\infty Abs(t) \cdot dt}(min^{-1}) \quad (3)$$

$$C(t) = C^o\tau\, E(t)(mol\, m^{-3}) \quad (4)$$

$$C^o\tau = \frac{n}{Q} = \frac{C_i\, V_{loop}}{Q} \quad (5)$$

$$\bar{t}_r = \int_0^\infty E(t) \cdot t\, dt\ \ (min) \quad (6)$$

3.4 Mathematical modelling

3.4.1 SFC-fixed bed

To be able to model and design a separation process such as a SF-TMB, it is necessary to know some properties about the compounds of interest that will be used in TMB columns and the influence of the operating conditions.

To be able to analyze and fit the dynamic responses to the inlet perturbations and estimate some parameters and properties of this system, a mathematical model of a fixed bed was developed in gPROMS' language [38]. The estimated parameters will be used in the TMB mathematical model.

Several assumptions and considerations were made, some of them typical of fixed bed columns and also of SFC-fixed bed columns [11, 39].

1) The fixed bed hydrodynamics is represented by the plug flow model with axial dispersion: axial dispersion plug flow.
2) The radial dispersion was neglected because the column radius is very small.
3) Column closed to diffusion: Danckwerts boundary conditions.
4) Overall isothermal process: no energy balance equations.
5) Constant fluid velocity, system pressure and temperature, adsorbent characteristics and packing along the column.
6) The mass resistance is well described by a Linear Driving Force model (LDF)
7) Adsorption is described by the Langmuir competitive equilibrium isotherm.
8) The adsorption equilibrium is reached instantaneously

Assumptions 4) and 5) were made because the equipment is able to maintain the velocity, temperature and pressure almost constant. Assumption 1) was made taking into account the visual form of the signals obtained. Assumptions 6) and 7) were made after the analysis of some experimental data and parameter estimation on gPROMS' software. Note that for the pulse experiences (monocomponent) the Langmuir competitive character reduces to a simple Langmuir adsorption isotherm.

Based on this, the material balance to an infinitesimal fraction of the column leads to the following partial differential equations. The variable z is the dimensionless column axial position $z = \frac{x}{L}$.

Mass balance fluid phase:

$$\frac{\partial C_{b,i}}{\partial t} + \frac{u}{L}\frac{\partial C_{b,i}}{\partial z} + \frac{1-\varepsilon_b}{\varepsilon_b}\frac{3\,k_L}{r_p}\left(C_{b,i} - \overline{C}_{p,i}\right) = \frac{1}{L^2}\frac{\partial}{\partial z}\left(D_{ax}C_T\frac{\partial y_i}{\partial z}\right) \quad (7)$$

Mass balance solid phase (particles):

$$\frac{\partial \overline{C}_{p,i}}{\partial t} + \frac{1-\varepsilon_p}{\varepsilon_p}\frac{\partial \overline{q}_i}{\partial t} = \frac{3\,k_L}{r_p}\left(C_{b,i} - \overline{C}_{p,i}\right) \quad (8)$$

Langmuir competitive adsorption isotherm:

$$\overline{q}_i = \frac{K_{ads,i}Q_{sat,i}\overline{C}_{p,i}}{1 + \sum_i K_{ads,i}\overline{C}_{p,i}} \quad (9)$$

Initial conditions:

$$t = 0\text{: } C_{b,i} = \overline{C}_{p_i} = q_i = 0 \quad (10)$$

Danckwerts Boundary Conditions:

$$z = 0\text{:} \qquad C_{b_i}^{in} = C_{b_i} - \frac{1}{Pe_i}C_T\frac{\partial y_i}{\partial z}\bigg|_{z=0} \quad (11)$$

$$z = 1\text{:} \qquad \frac{\partial C_{b_i}}{\partial z}\bigg|_{z=1} = 0 \quad (12)$$

In these equations, all the variables and parameters definitions follow the traditional nomenclature and can be found on the glossary.

Several transport and physical/chemical parameters as well as the adsorption isotherm parameters are required as input in the model. Some of these parameters were estimated using the gProms' tool parameter estimation, namely k_L k_{ads} and Q_{sat}. In order to reduce the number of parameters to be estimated, the remaining were taken from the literature or calculated using appropriated correlations as described below in the correlations subsection.

3.4.2 TMB

The results obtained from the mathematical modeling of the fixed-bed inlet concentration perturbations are used in the mathematical modeling of moving bed countercurrent chromatography, known as TMB.

A TMB is an equipment in which the solid moves in the opposite direction of the liquid. For an hypothetical binary mixture of compounds "A" and "B, where "A" is the more strongly adsorbed compound on the adsorbent surface, a traditional TMB with four zones is schematically represented in Figure 7 [40]. The SF-TMB can be generally described by a TMB, where instead of liquid streams, supercritical fluid streams are circulating.

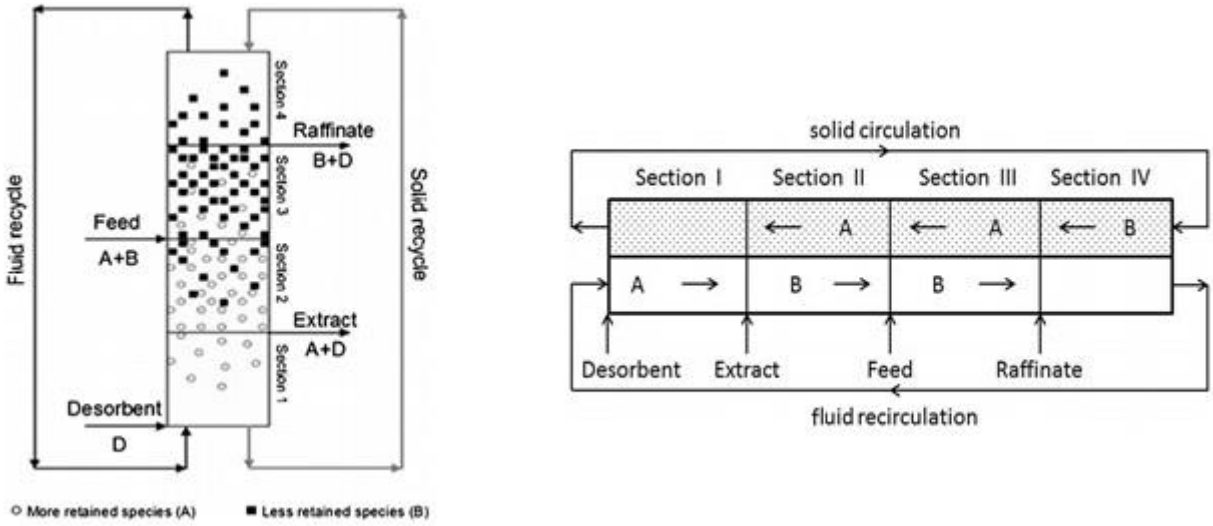

Figure 7 - Scheme of a TMB and the desired fluxes of each species to guarantee the complete separation. Adapted from [40].

The traditional TMB has two inlet and two outlet streams. The inlet streams are the desorbent, which would be $ScCO_2$, and the feed, which would be the mixture of solketal and water. The two outlet streams are the extract, where the more adsorbed product is collected (water), and the raffinate where the less adsorbed product (solketal) is collected [40].

The Feed stream (F), containing both compounds, is fed to the unit. While the compound "A" follows the adsorbent into Zone II towards the extract stream (X), the compound "B" is transported by convection into Zone III to the raffinate stream (R), allowing the separation of the compounds in two different streams diluted in the eluent (stream D). Zones I and IV are regeneration zones designed in order to avoid the contamination of the solid and the fluid recycling streams respectively [40].

So the four streams divide the unit into four different sections, each one with a specific role and different flow rates. In section I, the eluent flow rate should be high enough to regenerate the adsorbent through the desorption of "A" (more adsorbed species), before being recycled to section IV, avoiding its contamination. In section II, the desorption of the B should occur to avoid extract contamination. In section III, the adsorption of the A should occur to avoid raffinate contamination. In section IV, the fluid flow rate should be low enough to force the adsorption of "B", pushing it backwards, and guaranteeing that the fluid phase can be recycled without contaminating section I.

The following equations describe the steady-state model of a TMB with porous adsorbent particles. Considering the same assumptions made for the fixed bed column for each of the four columns of the TMB (j), the equations (15) to (19) are similar to SFC-fixed bed equations but now applied to each column. The mass balance to the solid phase takes now into account the solid movement by introducing the solid velocity u_s and the partial derivative in order to time is now equal to zero, this last is the same for equation (13) [11, 40].

Steady state mass balance in a volume element of the section j fluid phase:

$$\frac{u_j}{L}\frac{\partial(C_{b,i,j})}{\partial z}+\frac{1-\varepsilon_b}{\varepsilon_b}\frac{3}{r_p}k_{L,i}\left(C_{b,i,j}-\overline{C}_{p,i,j}\right)=\frac{D_{ax,j}}{L^2}\frac{\partial}{\partial z}\left(C_T\frac{\partial y_{i,j}}{\partial z}\right) \tag{13}$$

Steady state mass balance solid phase:

$$\frac{u_s}{L}\left(\varepsilon_p\frac{\partial\left(\overline{C}_{p,i,j}\right)}{\partial z}+(1-\varepsilon_p)\frac{\partial\left(\overline{q}_{i,j}\right)}{\partial z}\right)=\varepsilon_p\frac{3}{r_p}k_{L,i}\left(C_{b,i,j}-\overline{C}_{p,i,j}\right) \tag{14}$$

Langmuir competitive adsorption isotherm:

$$\overline{q}_{i,j}=\frac{K_{ads,i,j}Q_{sat,i}\overline{C}_{p,i,j}}{1+\sum_i K_{ads,i}\overline{C}_{p,i,j}} \tag{15}$$

Boundary conditions:

$$z=0 \qquad u_jC_{b_{i,j}}^{in}=u_jC_{b_{i,j}}-\frac{D_{ax,j}}{L}\left.\frac{\partial C_{b_{i,j}}}{\partial z}\right|_{z=0} \tag{16}$$

$$z=1 \qquad \left.\frac{\partial C_{b_{i,j}}}{\partial z}\right|_{z=1}=0 \tag{17}$$

$$(j=1{:}3) \qquad \left.\overline{C}_{pi,j}\right|_{z=1}=\left.\overline{C}_{pi,j+1}\right|_{z=0} \quad and \quad \left.q_{i,j}\right|_{z=1}=\left.q_{i,j+1}\right|_{z=0} \tag{18}$$

$$(j=4) \qquad \left.\overline{C}_{pi,4}\right|_{z=1}=\left.\overline{C}_{pi,1}\right|_{z=0} \quad and \quad \left.q_{i,4}\right|_{z=1}=\left.q_{i,1}\right|_{z=0} \tag{19}$$

Node balances:

Eluent node
$$\begin{cases} u_1 = u_4 + u_E \\ u_4\, C_{b,i,4}^{out} = u_1\, C_{b,i,1}^{in} \end{cases} \quad (20)$$

Feed node
$$\begin{cases} u_3 = u_2 + u_F \\ u_2\, C_{b,i,2}^{out} + u_F\, C_{b_{i,F}} = u_3 C_{b,i,3}^{in} \end{cases} \quad (21)$$

Extract node
$$\begin{cases} u_2 = u_1 - u_X \\ C_{b,i,1}^{out} = C_{b,i,2}^{in} = C_{b_{i,X}} \end{cases} \quad (22)$$

Raffinate node
$$\begin{cases} u_4 = u_3 - u_R \\ C_{b,i,3}^{out} = C_{b,i,4}^{in} = C_{b_{i,R}} \end{cases} \quad (23)$$

Regarding the determination of the optimum operating point, the approach followed in this work is based on the triangle theory. The TMB triangle separation region resumes the set of operating conditions that guarantee a complete separation of a binary mixture and the regeneration of the fluid and solid phases of a TMB [40].

To better describe the separation, let's first define γ_j as the ratio between the fluid and solid flow rates in each TMB zone and γ_F as the ratio between the fluid feed flow and solid flow rate:

$$\gamma_j = \frac{Q_j}{Q_s} \qquad (j = 1{:}\,4 \text{ and } F) \quad (24)$$

The separation region is obtained by representing γ_2 versus γ_3. For the equilibrium theory with linear isotherms, this leads to a rectangular triangle above the diagonal that represents the zero feed flow rate. On the same way, representing γ_4 versus γ_1 gives us a rectangular regeneration region [40].

Any conditions simultaneously inside the separation and regeneration zone guarantee a complete separation of a binary mixture with a TMB based on the assumption of instantaneous equilibrium. The vertex of the separation region is the point of maximum productivity, but due to the theoretical assumptions and variations that can occur, it should not be used as operating point. [40]

So, if it was assumed linear adsorption isotherm, instantaneous equilibrium and ideal flow a triangular separation region would be obtain. However, the system under study is non ideal, as there are strong mass transfer resistances, axial dispersion, nonlinear adsorption (Langmuir isotherm) and porous particles. As so, equations (25) to (27) are more general to provide a first guess of the separation and regeneration region. The coefficient β is a safety factor which is always bigger than 1 [40].

$$\gamma_1 > \beta \frac{(1-\varepsilon_b)}{\varepsilon_b}\left(\varepsilon_p + (1-\varepsilon_p)\frac{q_{A,1}}{\overline{C}_{p_{A,1}}}\right) \quad (25)$$

$$\frac{(1-\varepsilon_b)}{\varepsilon_b}\left(\varepsilon_p + (1-\varepsilon_p)\frac{q_{B,2}}{\overline{C}_{p_{B,2}}}\right) < \gamma_2 < \gamma_3 < \frac{(1-\varepsilon_b)}{\varepsilon_b}\left(\varepsilon_p + (1-\varepsilon_p)\frac{q_{A,3}}{\overline{C}_{p_{A,3}}}\right) \quad (26)$$

$$\gamma_4 < (1-\beta)\frac{(1-\varepsilon_b)}{\varepsilon_b}\left(\varepsilon_p + (1-\varepsilon_p)\frac{q_{B,4}}{\overline{C}_{p_{B,4}}}\right) \quad (27)$$

To numerically obtain the separation region, it is important to define some separation performance parameters. The performance parameters considered in this work are the raffinate (PUR_R) and extract purity (PUR_X), the productivity and the desorbent consumption, given by equations (28) to (31) respectively. The productivity (PR_R) and the desorbent consumption (DC_R) are referent to the raffinate stream as the component of interest is the solketal ("B"), less adsorbed by the solid phase [40].

Raffinate purity $$PUR_R = \frac{C_B^R}{C_A^R + C_B^R} \quad (28)$$

Extract purity $$PUR_X = \frac{C_A^X}{C_A^X + C_B^X} \quad (29)$$

Raffinate productivity $$PR_R = \frac{Q_R C_B^R}{(1-\varepsilon_b)\, V_c\, N_c} \quad \left[\frac{kg_{product}}{L_{ads}\cdot day}\right] \quad (30)$$

Desorbent consumption (referring to the raffinate) $$DC_R = \frac{Q_D}{Q_R C_B^R} \quad \left[\frac{L_{Desorbent}}{kg_{product}}\right] \quad (31)$$

Setting the intended extract and raffinate purity parameters, the separation region can be defined.

The γ_1 and γ_4 are previously fixed in order to ensure the regeneration of the solid and fluid phase in sections I and IV, given by equations (25) and (27).

Then, starting with the lowest possible γ_2 using the left part of equation (26) as an equality and starting with a very low γ_F, γ_3 is obtained from equation (21). The process is simulated with these operating conditions and the performance parameters are obtained. Then the values of γ_2 and γ_3 are increased (keeping the same (γ_F) step by step until the limits of the separation region (upper and lower) that obey to the purity constraint are found, like PUR_X, PUR_R >99%.

Afterwards the value of γ_F is increased gradually and the previous step repeated. In this way it is possible to numerically obtain the separation zone.

The TMB obtains high-purity product even using low selectivity adsorbents. However, the actual movement of the solid phase is hard to implement due to obvious technical problems such as the equipment abrasion, the erosion of the adsorbent and maintaining constant the solid flow. For these reasons, the technology used is the simulated moving bed, where the inlet /outlet ports of a series of packed bed columns are periodically shifted in the direction of the fluid flow, simulating the movement of the solid phase [40].

3.5 $ScCO_2$ properties and correlations

In this section it is presented important $ScCO_2$ properties for the development of this work and correlations to estimate solute-solvent interactions and specific mass-transfer properties.

Viscosity and Density

As the solvent used is pure $ScCO_2$ and the pulse injections are small quantities of solute, the obtained solution is diluted and so the solution viscosity and density can be considered only pressure and temperature dependent and their values can be found in the literature for similar operating conditions [13]. As the data available in literature for viscosity is not at the exact same conditions (pressures of 100, 150 and 200 bar and temperatures of 313.15, 333.15 and 353.15K), a 3rd polynomial adjust of $ScCO_2$ viscosity as function of the temperature was made for each pressure, described by equations (32) to (34) in order to be able to interpolate for the desired value.

$ScCO_2$ density values are found in the literature for the exact same conditions and are summarized in Table 5 [15].

$$\mu_{100bar} = -4.165 * 10^{-10}\mathrm{T}^3 + 4.358 * 10^{-7}\mathrm{T}^2 - 1.520 * 10^{-4}\mathrm{T} + 1.769 * 10^{-2} \quad (32)$$

$$\mu_{150bar} = 1.290 * 10^{-10}\mathrm{T}^3 - 1.191 * 10^{-7}\mathrm{T}^2 + 3.548 * 10^{-5}\mathrm{T} - 3.321 * 10^{-3} \quad (33)$$

$$\mu_{200bar} = 7.083 * 10^{-12}\mathrm{T}^3 - 1.375 * 10^{-9}\mathrm{T}^2 - 2.256 * 10^{-6}\mathrm{T} + 7.025 * 10^{-4} \quad (34)$$

Table 5 - Density (kg m^{-3}) values for pure $ScCO_2$ at the working conditions [15].

Operating conditions	100 bar	150 bar	200 bar
313.15 K	628.59	780.25	839.80
333.15 K	289.95	553.73	691.70
353.15 K	221.60	427.15	593.91

Molecular Diffusion

Taking into account the assumption previously mentioned, the diluted diffusion coefficients of solute (1) diluted in the solvent (2) (D_{12}) can be calculated by the Wilke and Chang correlation described by equation (35). It was used a modified version adjusted specifically for $ScCO_2$ diluted solutions in the condition range 74 < P < 400 bar and 303.15 < T < 373.15K [41].

$$D_{12} = 8.6 * 10^{-15} \frac{T M_2^{1/2}}{\mu_2 V_{M,i}^{0.6}} \quad (35)$$

In equation (35), T (K) is the absolute operating temperature, M_2 (g mol^{-1}) is the molecular weight of the solvent, $V_{m,i}$ (cm^3 mol^{-1}) is the solute molar volume at normal boiling point and μ_2 is the solvent viscosity (Pa). Values may be found in Table 1.

Axial Dispersion

The axial dispersion, D_{ax}, provides an idea of the deviation from the ideal plug flow. Pe_p number and D_{ax} are related by equation (36).

$$Pe_p = \frac{u\, d_p}{D_{ax}} \quad (36)$$

In Table 6 it is summarized correlations to obtain Pe_p (equations (39) to (44)) or directly the D_{ax} (TanLiou correlation, equation (45)). Except TanLiou, all correlations are function of Reynolds (Re) and/or Schmidt (Sc) dimensionless numbers, calculated by equations (37) and (38) respectively. Re and Sc numbers are directly or indirectly functions of the operating temperature and pressure turning them different for each operating condition. Sc is also function of D_{12} that is different to each compound, so Sc also depends on the compound study.

So, the correlations depend on the compound and operating conditions, except the Catchpole, Tan Liou and Chung When correlations, which are only functions of Re and so independent of the compound's physical properties.

The correlations of Edwards-Richardson and Hsu-Haynes were designed and tested for gases, while Wakao and Chung-Wen studied liquid systems in porous media. Yet, Catchpole, Funazukuri and Tan-Liou studied the axial dispersion in $ScCO_2$ through fixed bed tests.

Funazukuri et. Al (1998) [42] reported that the axial Péclet numbers obtained for small particles (d_p<1 mm) were an order of magnitude lower than literature data for gases and liquids at ambient pressures.

$$Re = \frac{u0\ d_p\ \rho}{\mu} \tag{37}$$

$$Sc = \frac{\mu}{\rho\ D_{12}} \tag{38}$$

Table 6 - Correlations for estimation of the axial dispersion in a fixed bed column.

Authors	Correlation	Type of fluid and operation range	Eq.	Ref
Edwards-Richardson	$\frac{1}{Pe_p} = \frac{0.73}{Re\ Sc} + \frac{1}{2 + 18.98\ (\mathrm{Re\ Sc})^{-1}}$	Gases	(39)	[43]
Hsu-Haynes	$\frac{1}{Pe_p} = \frac{0.328}{Re\ Sc} + \frac{3.33}{1 + 0.59\ (\mathrm{Re\ Sc})^{-1}}$	Gases	(40)	[43]
Chung-Wen	$Pe_p = \frac{1}{\varepsilon_b}(0.20 + 0.011\ Re^{0.48})$	Liquids 10^{-3}<Re<10^3	(41)	[44]
Wakao	$\frac{1}{Pe_p} = 0.5 + \frac{20}{Re\ Sc}$	Liquids	(42)	[43]
Catchpole	$\frac{1}{Pe_p} = \frac{0.018}{Re} + \frac{10}{1 + 0.7\ Re^{-1}}$	$ScCO_2$ 100<P<300 bar ;313<T<333K 2<Re<80	(43)	[45]
Funazukuri	$\frac{1}{Pe_p} = \frac{D_{12}}{d_p\ u_0}\ 1.317\ (Re\ Sc)^{1.392}$	$ScCO_2$	(44)	[42]
Tan-Liou	$D_{ax} = 0.085\ u^{0.914} d_p^{0.388} \rho_r^{0.725} \mu_r^{0.676}$	$ScCO_2$ $0.3 < \left(\frac{Re}{\varepsilon_b}\right) < 30$	(45)	[46]

4 Results and Discussion

4.1 Pulse experiments

The data obtained from the experimental SFC-FB runs described in Table 4 is analyzed as described in section 3.2.1 - "Experimental procedure (pulse experiments)" and the results summarized in Table 7, Table 8 and Table 9.

Majewski et. al (2005) [10] studied and reported the influence of the operating temperature, pressure and cosolvent feed (this last one not directly studied in this work) on the $\overline{t}_r$ in a SFC system, specifically with $ScCO_2$ as solvent:

- Increasing the co-solvent feed tends to increase the polarity of the eluent, decreasing the $\overline{t}_r$ and selectivity, behavior identical to a traditional HPLC at normal phase conditions.

-In a SFC system, increasing the temperature tends to increase the $\overline{t}_r$, a contradictory behavior to the observed in a HPLC. The adsorption process is exothermic and taking into account the thermodynamics of the retention phenomena described by Gibbs equation, the increasing temperate is unfavorable to the adsorption process, leading to o a lower $\overline{t}_r$. However, temperature has an antagonistic effect in SFC systems as the CO_2 density drastically decrease with temperature, reducing the dissolution power and so increasing the $\overline{t}_r$.

-About the pressure, there is no effect on the eluent HPLC strength, as liquid are almost incompressible. Though, in supercritical conditions, the solvent density and consequential the dissolution power strongly increases with pressure, reducing the selectivity and the $\overline{t}_r$.

Concerning with the experimental data and results, it is important to observe some important situations and limitations. It is expected to acquire the absorbance signal, measured by an UV flux cell detector with a photodiode array detector, at the maximum absorption wavelength (λ_{max}) of the compound, which can be found in literature. However, the detector has a maximum reading capacity so, around λ_{max}, the signal is likely to saturate, especially for larger volume loop injections, which considerably increases the errors associated with the measurement. Also, the signal increase with concentration could be nonlinear, leading to false relations between data. In general, acetone and solketal signals are clear and noise free, contrasting with water signal, which is much less intense and with a lot of noise.

For acetone, the theoretical (see Appendix 3) and experimental λ_{max} in the UV/VIS region is about 270 nm [47]. Yet, the signal often saturates and so the signal acquisition was made at 230 nm, because at that wavelength the signal never saturates, has low noise and linear response to the concentration range studied.

For solketal, the theoretical λ_{max} (see Appendix 3) in the UV/VIS region is below 220 nm and also around 270 nm [48]. Nevertheless, in analysis made in our system, the λ_{max} readable was found at 270 nm, which never saturates for the volumes used. However, the signal response to concentration was not linear and so the wavelength 220 nm was choose although it led to higher noise interference and, consequently, slightly higher integration errors.

Studying water pulses was somewhat more difficult because water barely absorbs in the UV/VIS region (see Appendix 3) [49]. After some preliminary test it was chosen the wavelength 196 nm, almost in the low limit of the detector (190 nm). Initially, the equipment had an ELSD detector more capable of analyzing water injections but its calibration and operation was not successful.

There were also a lot of reproducibility problems, especially with water pulse injections, making it difficult to understand which are the most realistic and reliable results and requiring several injection repetitions. Some consecutive injections of the same compound, volume and operating conditions, with enough time between them for adsorbent regeneration, have different signal intensity, usually the second lower than the first and so on, and sometimes a totally different profile. There were even some injections with no signal response but noise, like if no compound was injected, especially for water injections and for small volumes like 10 and 50 µl. This raised some suspicions about the autosampler injections precision but they were not confirmed. To be sure that the acquisition wavelength and pulse experiences chosen to analyze were concordant, the area below the absorbance curve was analyzed, by integrating the absorbance with time and assessing the quantity injected or more precise the quantity read by the UV detector. An extensive analyzes to all data for each compound was made, and the best results are represented in Figure 8, confirming the linear signal response with concentration.

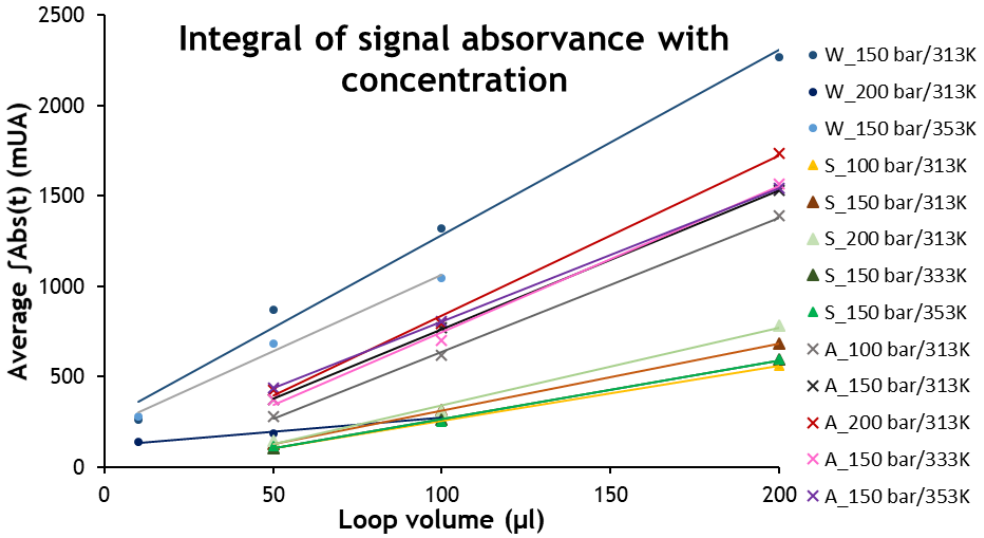

Figure 8 - Average injected amount for each compound for all loops and operating conditions. Only valid data is represented, the outsider points were not considered.

Taking these considerations into account, injections with similar curve form, $\bar{t}_r$ and quantity injected are considered to be more precise and validated. For some cases 12 pulse injections apparently valid were analyzed.

The $\bar{t}_r$ results are summarized in Table 7, Table 8 and Table 9 for solketal, acetone and water pulse injections respectively, for all concentrations and operating conditions studied. There are three main ways to analyze the following tables: the reference operating condition is the pressure set at 150 bar and temperature at 313 K. Then it was analyzed the influence of raising the temperature, changing the pressure and the injection volume. Pulse injections at 100 bar and 313 K were found to have much more noise and lower reproducibility than at 150 and 200 bar. In the same way, the results at 333 K and 353 K have more noise and lower signal intensity that at 313 K.

So, when contradictory results are obtained, concerning the pressure effect, the tendency shown from 150 to 200 bar will be considered valid. Regarding the temperature effect, in case of doubt the tendency shown from 313 K to 353 K should be considered, because the difference for the extremes to the intermediate 333 K may not be enough to clearly show the real tendency of $\bar{t}_r$ with temperature.

Table 7 – Summary of $\bar{t}_r$ (min) for solketal pulse injections (runs of 45 min) in different operating conditions – loop volume (µl) versus temperature (K) and pressure (bar).

Volume (µl)	100 bar/313 K	150 bar/313 K	200 bar/313 K	150 bar/333 K	150 bar/353 K
50	4.24 ± 0.48	4.19 ± 0.36	4.00 ± 0.17	5.03 ± 0.92	5.62 ± 0.14
100	2.57 ± 0.14	3.06 ± 0.15	2.79 ± 0.05	3.20 ± 0.28	3.46 ± 0.20
200	2.16 ± 0.02	2.14 ± 0.03	2.07 ± 0.05	1.97 ± 0.21	2.95 ± 0.18

Analyzing Table 7, regard to loop injection volume and so concentrations (as the eluent feed flow is constant), solketal $\bar{t}_r$ decreases with the increasing concentration for all operating conditions, supporting the decision of fitting the results to a Langmuir adsorption isotherm model.

Regarding the temperature, solketal $\bar{t}_r$ generally increases with temperature, which agrees with the tendency observed by Majewski et. al (2005) [10]. For the 50 µl loop, the temperature effect is accentuated, while for 100 µl and 200 µl is subtler. The only exception is for the 200 µl pulse at 333 K, with the $\bar{t}_r$ decreasing compared to the lowest temperature 313 K, yet within the experimental error.

Concerning the pressure, the $\bar{t}_r$ for 50 µl pulses shows a smooth decreasing tendency just like Majewski, Valery [10] reported, like for 200 µl pulses although showing an even smoother tendency. For 100 µl pulses, the $\bar{t}_r$ shows a decreasing tendency from 150 to 200 bar, but not from 100 to 150 or 100 to 200 bar. However, as previously mentioned, data at 150 and 200 bar is more reliable and the tendency from 150 to 200 bar is considered valid.

Table 8 – Summary of $\bar{t}_r$ (min) for acetone pulse injections (runs of 25 min) at different operating conditions – loop volume (µl), temperature (K) and pressure (bar).

Volume (µl)	100 bar/313 K	150 bar/313 K	200 bar/313 K	150 bar/333 K	150 bar/353 K
50	2.79 ± 0.34	2.02 ± 0.31	2.52 ± 0.05	2.67 ± 0.05	3.44 ± 0.22
100	1.43 ± 0.13	1.68 ± 0.08	1.57 ± 0.02	1.60 ± 0.19	2.18 ± 0.10
200	0.94 ± 0.03	1.25 ± 0.04	1.36 ± 0.01	1.24 ± 0.01	1.54± 0.13

For acetone, (Table 8), regarding the pulse concentration, the $\bar{t}_r$ decreases with concentration for all the operating conditions, just like for solketal, supporting the decision of fitting the results to a Langmuir adsorption isotherm model. With respect to temperature, $\bar{t}_r$ generally increases with temperature just like for solketal and like Majewski et. al (2005) [10] observed. The only exceptions are for the 100 and 200 µl loop from 313 K to 333 K, yet within the experimental error and, as discussed above, it is not relevant compared to the tendency shown from 313 K or 333 K to 353 K. The tendency due to different operating pressures is not clear and contradictory when analyzing different concentrations, concluding that pressure has almost no effect on acetone $\bar{t}_r$ or that its effect is faded by the experimental error.

Table 9 – Summary of $\bar{t}_r$ (min) for water pulse injections (runs of 90 min) in different operating conditions – loop volume (µl) versus temperature (K) and pressure (bar).

Volume (µl)	150 bar/313 K	200 bar/313 K	150 bar/353 K
10	19.00 ± 0.30	12.42 ±0.07	9.88 ± 0.16
50	17.79 ±1.43	14.59 ± 0.47	10.14 ± 0.26
100	16.67 ± 2.04	12.35 ± 0.43	8.71 ± 1.7
200	14.02 ± 1.38	-	-

In the case of water (Table 9), there is no reliable experimental data obtained for 200 µl pulse injections at 313 K and 200 bar and at 353 K and 150 bar due to experimental problems like the formation of two peaks, the second with a unusual form and at all wavelength (probably a flow perturbation) or the sudden pressure rising with ABPR closing and system shut down, most likely due to ice formation at the depressurizing time.

First, it is verified that the zeolite adsorbs much more water than solketal or acetone.

For all water concentrations pulses, $\overline{t}_r$ drastically decreases with increasing with pressure as well as with temperature. This behavior agrees with Majewski et. al (2005) [10] results for pressure but not for temperature. This may be explained by the major importance of water adsorption process (an exothermic phenomena) compared to the eluent effect.

Regarding the concentration, looking for the reference operating conditions there is a trend that indicates Langmuir adsorption. For 200 bar and 313 K and for 150 bar and 353 K, it is considered the tendency shown between 50 µl and 100 µl pulses, because for 10 µl the signal was particularly weak and the noise and tail influence on the $\overline{t}_r$ that may not allow a correct analysis.

By the $\overline{t}_r$ of the three compounds, it can be experimentally concluded that the zeolite HBEA-25 has a higher affinity to water rather than for solketal and acetone, as already expected. The most important reason relies on geometric factors: the zeolite HBEA-25 micropores have an average diameter of 5.1 Å (Table 2), the critical diameter (width) foe water is 1.93 Å, for CO_2 is 2.80 Å and for acetone is 3.08 Å, while solketal projection diameter ranges from 6.96 to 9.48 Å (Table 1). So, most probably solketal cannot access the micropores and it only adsorbs in the macropores, while water can perfectly diffuse inside the zeolite macro and micropores and consequently the zeolite strongly adsorbs water. Acetone has an intermediate size between water and solketal, close to the average micropores diameter, and its diffusion inside the smaller micropores might be hindered.

4.2 Parameter estimation

As already discussed, some variables are somewhat more difficult to obtain empirically or analytically. Hence, a more expedite method is used to predict them, by using the gPROMS parameter estimation tool, based on the maximum likelihood function.

The optimization is progressive, using the previously optimal results as the initial guess of the next parameter estimation to help the method convergence. Hence, the parameters estimated are the k_L, K_{ads} and Q_{sat}, which results are summarized in Table 10.

As alternative, in order to reduce the number of estimated parameters, the k_L was obtained considering the contribution of both external an internal mass transfer coefficients calculated by correlations (see Appendix 4). Nevertheless, the deviations between the model and the experimental data were higher, so the k_L was estimated by gPROMS' parameter estimation.

As the parameter estimation for three or four pulse concentrations at the same time for each compound and operating conditions takes a long computer calculation time, only some operating conditions were used for the estimations: the reference operating condition (150 bar and 313 K) for all compounds and concentrations and data at 150 bar and 353 K and at 200 bar and 313 K, in order to study respectively the temperature and pressure effect as these set of results better describe the operating conditions effect on the pulses, as previously discussed.

As the gPROMS' parameter estimation optimizes the residuals, the pulse experimental tails were previously cut to only analyze the initial, dynamic part of the pulse. If the complete tails were taken into account, the gPROMS totally fails to describe the experimental results.

The experimental pulse and the one predicted by the SFC-FB model for acetone, solketal and water pulses are displayed in Figure 9, Figure 10 and Figure 11, respectively. As the water $\bar{t}_r$ is higher than solketal's and acetone's, the analysis to water pulses data was longer than for solketal and acetone data. Water pulses at 150 and 313 K and at 200 bar and 313 K (runs 31 to 37) were analyzed until 2000 s, while runs 38 to 40 (water at 150 bar and 353 K) were analyzed until 1500 s. Acetone (runs 4 to 9 and 13 to 15) and solketal (runs 19 to 24 and 28 to 30) pulses data were analyzed until 200 s.

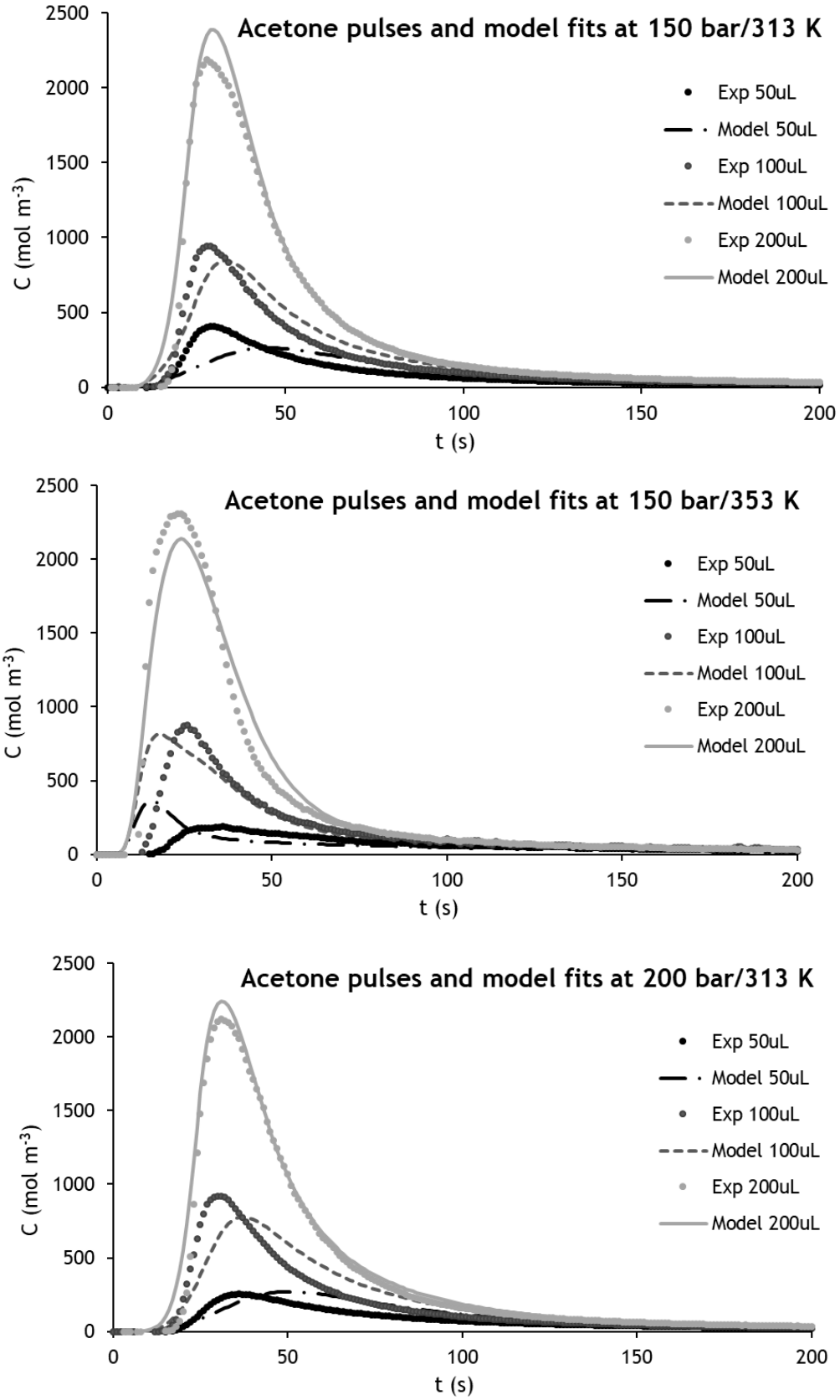

Figure 9 - Experimental C(t) data and correspondent adjusted curve with SFC-FB gPROMS' model for **acetone**. From the top to the bottom: at 150 bar/313 K; 150 bar/353 K; 200 bar/313 K. The estimated k_L, K_{ads} and Q_{sat} parameters resulting from this fit are summarized in Table 10.

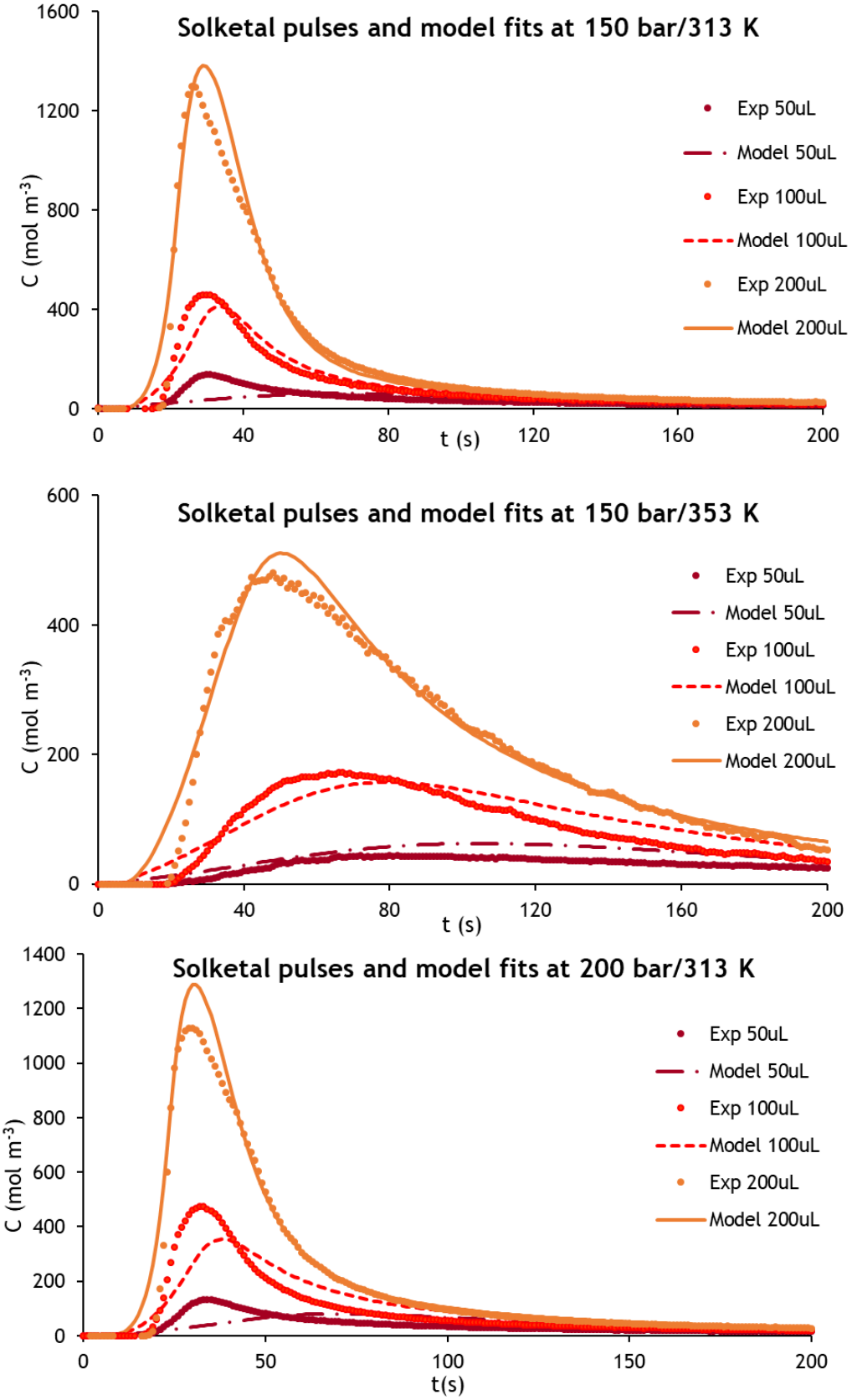

Figure 10 - Experimental C(t) data and correspondent adjusted curve with SFC-FB gPROMS' model for **solketal.** From the top to the bottom: at 150 bar/313 K; 150 bar/353 K; 200 bar/313 K. The estimated k_L, K_{ads} and Q_{sat} parameters resulting from this fit are summarized in Table 10.

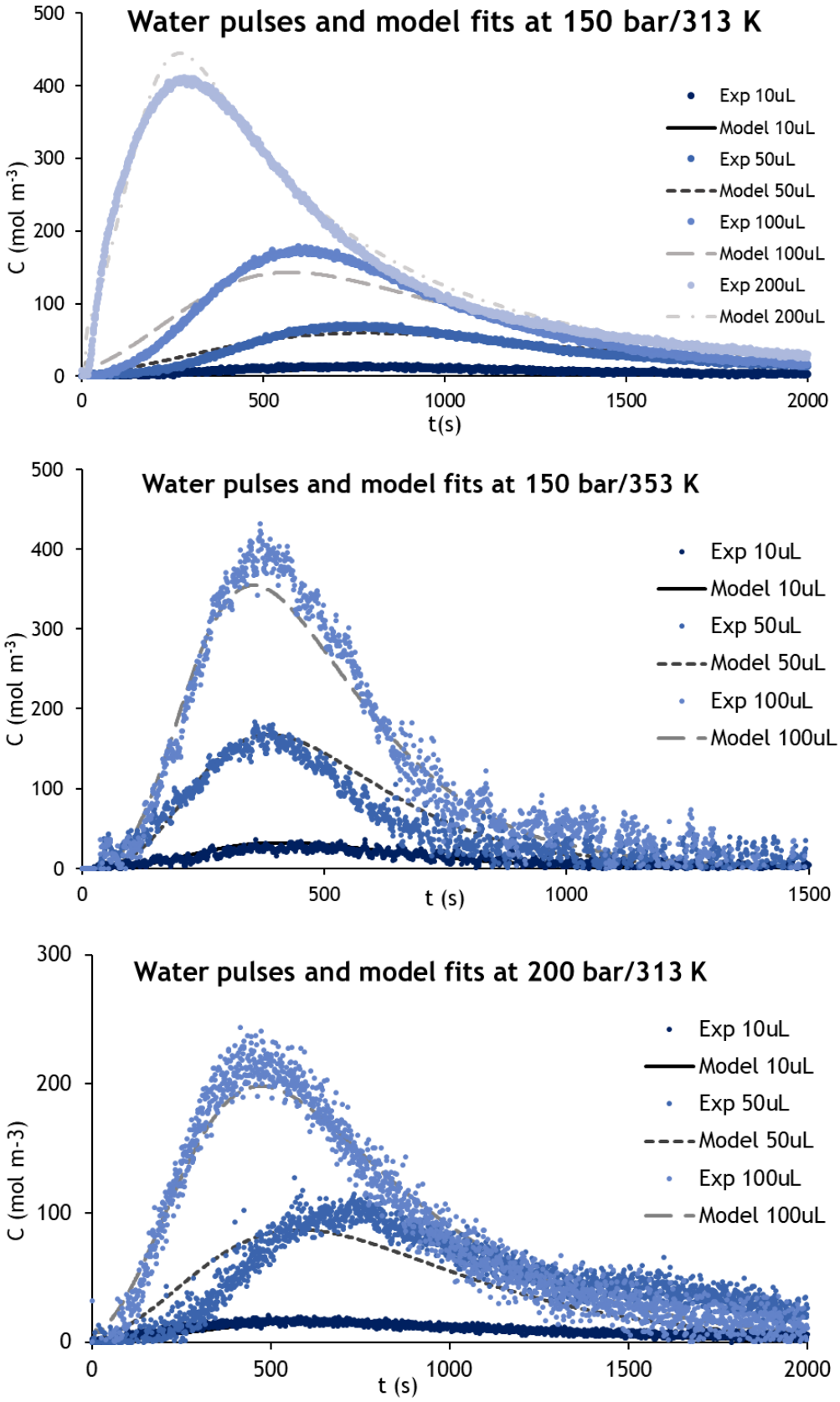

Figure 11 – Experimental C(t) data and correspondent adjusted curve with SFC-FB gPROMS' model for **water.** From the top to the bottom: at 150 bar/313 K; 150 bar/353 K; 200 bar/313 K. The k_L, K_{ads} and Q_{sat} parameters resulting from this fit are summarized in Table 10.

Table 10 – Estimated k_L (m s^{-1}), K_{ads} (m^3 mol^{-1}) and Q_{sat} (mol m$_{sol.}^{-3}$) for **acetone** (runs 4 to 9 and 13 to 15)**; solketal** (runs 19 to 24 and 28 to 30) **and water** (runs 31 to 40) at **150 bar/313 K**, **200 bar/313 K** and **150 bar/353 K**, using all concentrations pulses.

Compound	Operating conditions	k_L (m s^{-1})	K_{ads} (m^3 mol^{-1})	Q_{sat} (mol m$_{sol.}^{-3}$)
Acetone	150 bar / 313 K	4.89×10^{-5}	3.39×10^{-3}	1499
	150 bar / 353 K	9.59×10^{-6}	2.15×10^{-2}	938
	200 bar / 313 K	7.71×10^{-5}	2.18×10^{-3}	2051
Solketal	150 bar / 313 K	4.10×10^{-5}	2.57×10^{-2}	843
	150 bar / 353 K	4.89×10^{-5}	2.86×10^{-3}	3112
	200 bar / 313 K	5.49×10^{-5}	1.12×10^{-2}	1084
Water	150 bar / 313 K	6.24×10^{-5}	2.07×10^{-2}	35156
	150 bar / 353 K	1.43×10^{-4}	1.02×10^{-3}	105342
	200 bar / 313 K	7.19×10^{-5}	2.61×10^{-4}	47965

With the results obtained by parameter estimation, the Langmuir isotherms were obtained for acetone, solketal and water at three different operating conditions and they were assumed to be valid for the studied concentration range. In a general analyzes, it is notable that temperature as a major effect on the isotherm adsorption capacity unlike pressure. The most important conclusion is that the zeolite HBEA-25 strongly adsorbs water rather than acetone or solketal, independently of the operating conditions, as it was expected because of zeolite HBEA-25 high selectivity for water.

Analyzing the water results, for the studied concentration range, the zeolite strongly adsorbs at 150 bar and 313 K. This is in accordance with the $\overline{t}_r$ analyzes (Table 9), where it is shown the pronounced influence of the concentration on the $\overline{t}_r$ .The zeolite capacity reduces either with increasing pressure or temperature in the concentration range tested. At these conditions the isotherm presents an almost linear behavior. This may be a consequence of $ScCO_2$ competitive adsorption become more significant with the increasing pressure or temperature. Nevertheless, analyzing the extrapolated isotherms to higher concentrations, the zeolite eventually saturates for higher water concentration.

For solketal, as expected and discussed above for the $\overline{t}_r$ described in Table 7, the behavior follows the one described by Majewski, Valery [10] for SFC. Notice that the isotherms predict the zeolite saturation at low solketal concentrations. In a more tangible unit, at about 1 mol/L the HBEA-25 is practically saturated, at 313 K for both pressures.

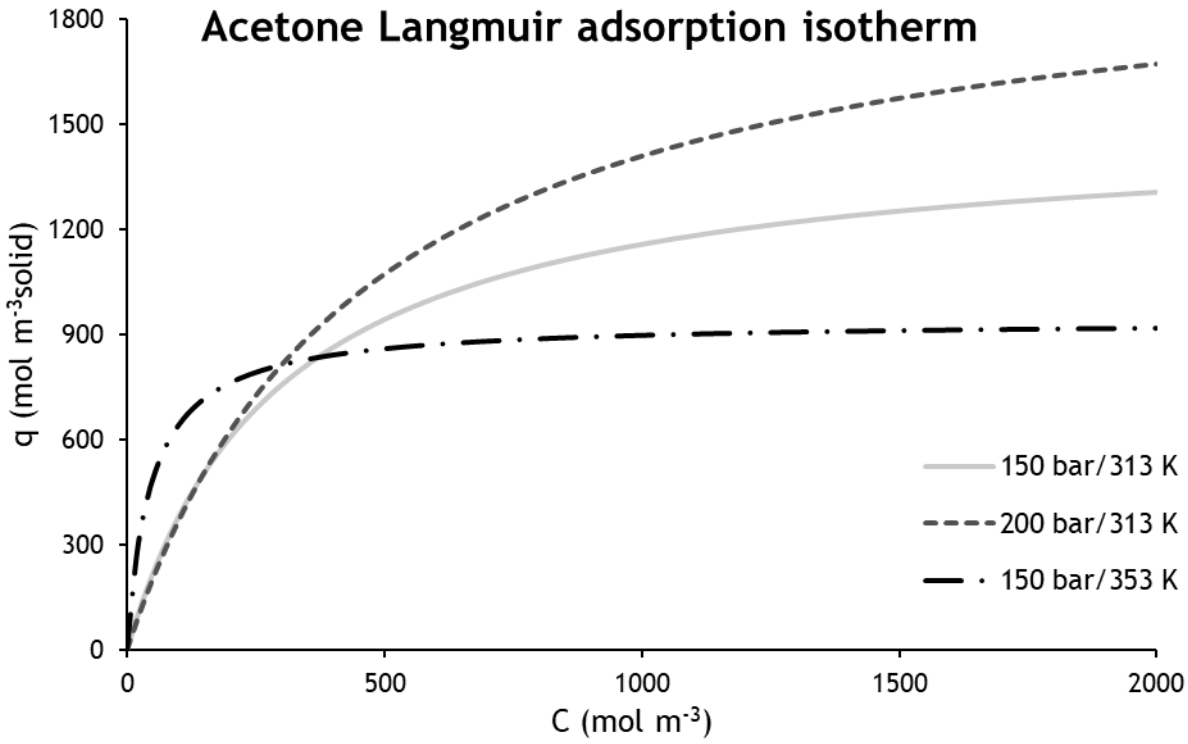

Figure 12 - Acetone Langmuir adsorption isotherm at the studied concentrations, at the three operating conditions simulated, using the Langmuir constants K_{ads} and Q_{sat} in Table 10.

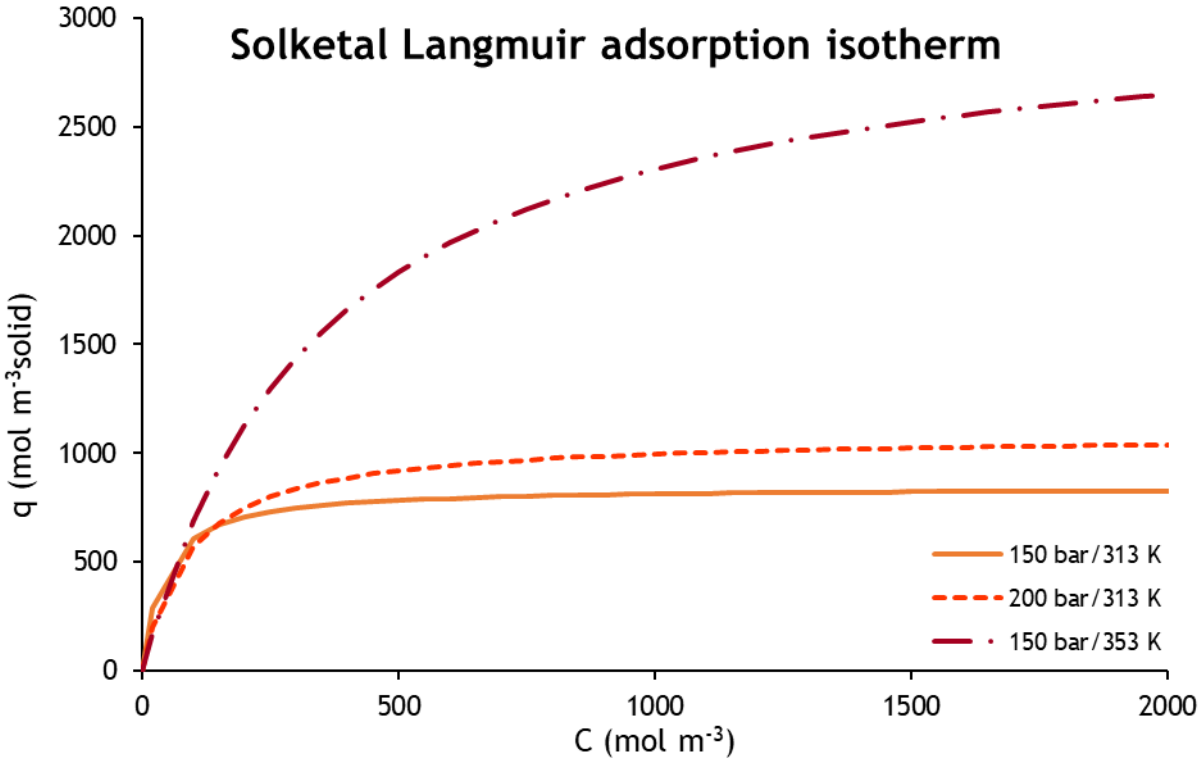

Figure 13 – Solketal Langmuir adsorption isotherm at the studied concentrations, at the three operating conditions simulated, using the Langmuir constants K_{ads} and Q_{sat} in Table 10.

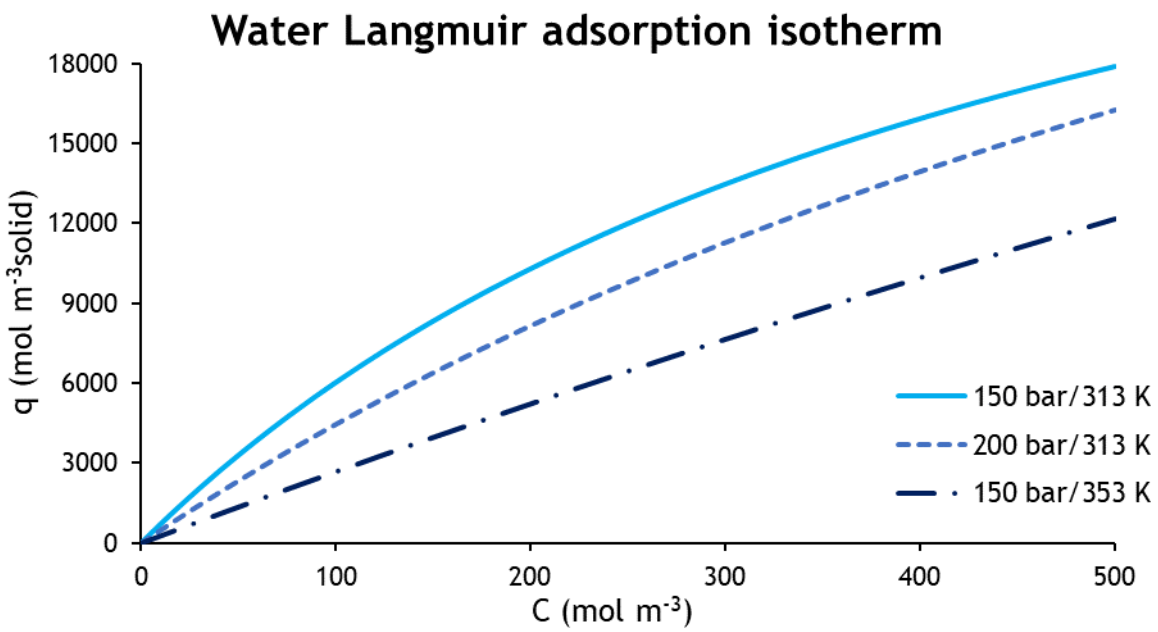

Figure 14 – Water Langmuir adsorption isotherm at the studied concentrations, at the three operating conditions simulated, using the Langmuir constants K_{ads} and Q_{sat} in Table 10.

The estimated k_L values also follow the expected trend with water presenting the highest value independently of the conditions tested. The mass transfer is enhanced with temperature according to the parameters estimated for water and solketal. The same was not verified for acetone; however, the value estimated for 150 bar and 353 K seems to be an outlier. The effect of pressure in the mass transfer is lower but all k_L values increased with pressure.

4.3 TMB simulation

Although SF-TMB may work in a pressure/temperature gradient mode, in this work it was only studied and simulated the simpler isocratic, isobaric and isothermal operating mode. The feed is constituted by a binary and equimolar mixture of solketal and water. The composition of the feed stream was set to the maximum value measured in the pulse experiments in order to ensure the validity of the adsorption and mass transfer parameters previously estimated.

First, it is important to mention that the design of a TMB is an iterative process, so a lot of hypotheses were tested in order to achieve the more realistic results and optimize the process with the data available from the SFC-FB experiences. As a first approach, the reference operating condition 150 bar and 313 K was simulated. Then, the operating conditions 200 bar/313 K and 150 bar/353 K were tested.

A four zones SF-TMB with equal sized columns was simulated. To be able to use the data obtained from the SFC-FB experiences, the same adsorbent, column packaging, operating conditions and similar column diameter were considered. To work in a more acceptable scale, have better performance and to guarantee that there is enough residence time so that mass transfer problems could be minimized, columns with 0.375 m length were simulated. The performance parameters PUR_R and PUR_X were set in a minimum of 99 %.

The u_s for each operating condition was defined in such a way that the average Q_{II} and Q_{III} were about the same as the volumetric flow rate of the pulse experiments (2 ml min^{-1}) so that k_L values for water and solketal are still valid. At 150 bar and 313 K and at 200 bar and 313 K, the u_s was 0.75 cm min^{-1}, while at 150 bar and 353 K the u_s was 3.75 cm min^{-1}.

In a TMB, it is likely that in zones II and III the adsorption between the water and solketal is competitive. As multicomponent pulse tests in the SFC-FB column were not performed, due to difficulty in properly reading the two signals as water barely absorbs comparing to solketal in the UV/VIS region, three scenarios were established:

1) Langmuir adsorption model (no competition)
2) Competitive Langmuir adsorption model
3) Dual site competitive Langmuir adsorption model

The water and solketal K_{ads} and Q_{sat} used to describe the isotherms are the ones summarized in Table 10.

Simulating a TMB model with a simple Langmuir adsorption model for both compounds gives a separation region; however, it would not be correct to assume that both solketal and water do not compete in the adsorption process for the zeolite's active centers in zone II and III.

Considering a simple competitive adsorption for each compound results in almost no separation region. The reason for this can be seen in Figure 15, in which the competitive (50/50% mixtures) adsorption isotherm is compared with the single component isotherm. A large decrease on the water capacity is verified. However, by the pulse experiences results, it is known that the zeolite adsorbs much more water than solketal and it should not be expected that the presence of solketal (that adsorbs much less) has such a high effect on the zeolite capacity for water.

So, a better model to describe the adsorption process for these compounds may be required. Considering the bifurcated water sorption behavior reported by Loughlin (2009) [50] in aluminosilicate zeolite 4A, a pseudo unit with two different size cavities type, α and β, both accessible to water, and its similarities with the zeolite HBEA-25, a dual site competitive adsorption model, given by equation (46), may better describe the water sorption phenomena. This model is also proposed by Guiochon et al. (2006) [51].

Now, knowing that zeolite HBEA-25 quickly saturates for solketal and that solketal has difficult in access micropores compared to water due to size differences, this model assumes that solketal only adsorbs in macropores, competing with water, resulting in a Langmuir competitive model, given by equation **(47)**. As previously defined, water is the compound "A", most adsorbed by the solid. The fraction α is referred to macropores while $(1-\alpha)$ goes for micropores, where α is calculated by equation **(48)**.

$$\overline{q}_A = \alpha \frac{K_{ads,A} Q_{sat,A} \overline{C}_{p,A}}{1 + \sum_i K_{ads,i} \overline{C}_{p,i}} + (1-\alpha) \frac{K_{ads,A} Q_{sat,A} \overline{C}_{p,A}}{1 + K_{ads,A} \overline{C}_{p,A}} \quad \textbf{(46)}$$

$$\overline{q}_B = \frac{K_{ads,B} Q_{sat,B} \overline{C}_{p,B}}{1 + \sum_i K_{ads,i} \overline{C}_{p,i}} \quad \textbf{(47)}$$

$$\alpha = \frac{A_{macropores}}{A_{pores,total}} \quad \textbf{(48)}$$

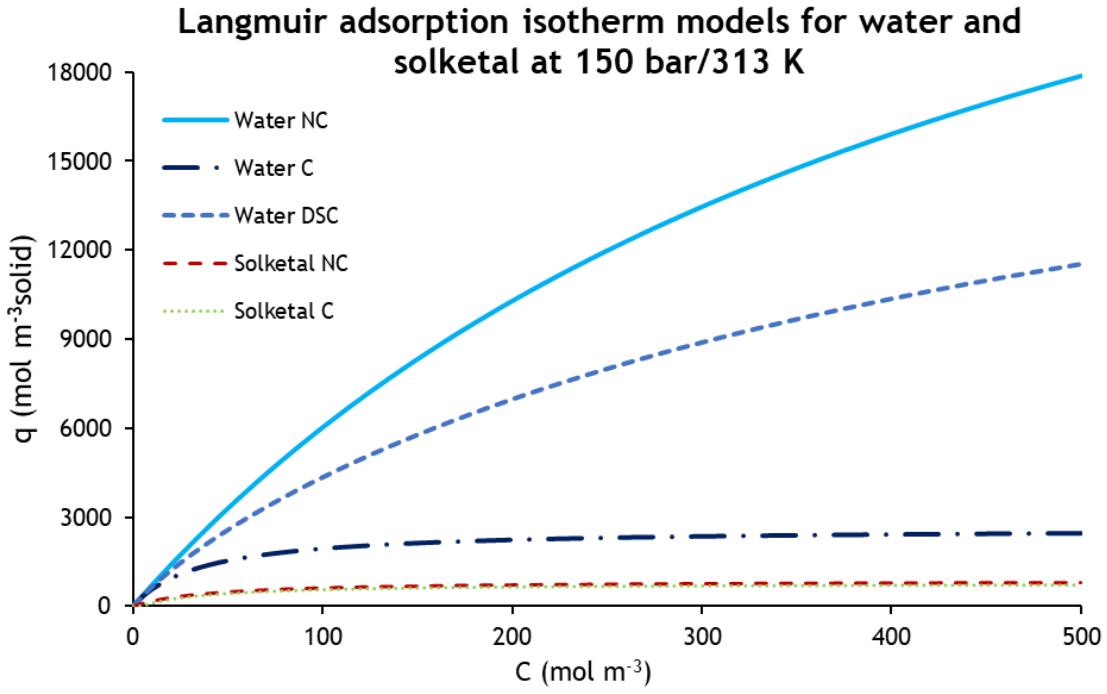

Figure 15 – Comparison of the water and solketal Langmuir adsorption isotherms at 150 bar and 313 K: water noncompetitive (NC); water competitive (C); water dual site competitive (DSC); solketal noncompetitive (NC); solketal competitive (C); α = 0.412. K_{ads} and Q_{sat} parameters may be found on Table 10.

Before obtaining the final SF-TMB operating conditions, it is crucial to guarantee a complete solid and fluid regeneration. Equations (25) and (27) were used to properly define the regeneration zones fluid and solid flow rate ratios. Having in mind the TMB operation mode and De Vault's equation (1943), in zone I the water needs to be desorbed from the solid to the fluid phase in order to regenerate the solid and move water back to zone II. As the water adsorption follows a Langmuir isotherm model, for the desorption a dispersive wave is formed. So, in zone I, low water concentrations may be found and the Langmuir adsorption isotherm may approximate to a Henry (linear) isotherm $q = K'C$, where $K' = Q_{sat,A}K_{ads,A}$.

Now, zone IV purpose is to regenerate the fluid phase and to obtain recyclable clean eluent, so solketal may return back with the solid to zone III. As only solketal, at relatively high concentrations, is present in zone IV (water may not reach the raffinate stream), a simple Langmuir adsorption isotherm (equation (9)) may be valid to describe the shock wave. The solketal concentration considered is approximated by the pure solketal feed concentration.

Depending on the operating concentrations, and consequently the parameters used, the values of β used to guarantee the solid and fluid regeneration were different. At 200 bar/313 K a β = 0.2; at 150 bar/313 K a β = 0.3 and at 150 bar/353 K a β = 0.4 was considered in order to complete regenerating of Zone I and Zone IV.

With the regeneration zone flow rate ratios properly defined after applying an adequate safety factor to account for the mass transfer resistances, the separation region and the performance parameters for the three Langmuir adsorption isotherms hypotheses at the three operating conditions were obtained using the SF-TMB model, following the procedure described in section 3.4.2 - "Mathematical modelling: TMB" and setting the performance parameters PUR_R and PUR_X minimum of 99 %. A summary of the TMB operating parameters is present in Table 11. The separation regions for the three operating conditions simulated comparing the three Langmuir adsorption equilibrium models tested are graphically represented in Figure 16 to Figure 18, whereas the estimated performance parameters PR_R and DC_R are summarized in Table 12.

Table 11 - Operating parameters for the TMB.

TMB parameters	Value
$\boldsymbol{\varepsilon_b}$	0.438
$\boldsymbol{\varepsilon_p}$	0.326
L (m)	0.375
$\boldsymbol{N_c}$	4
$\boldsymbol{PUR_R/PUR_X}$ **(%)**	99

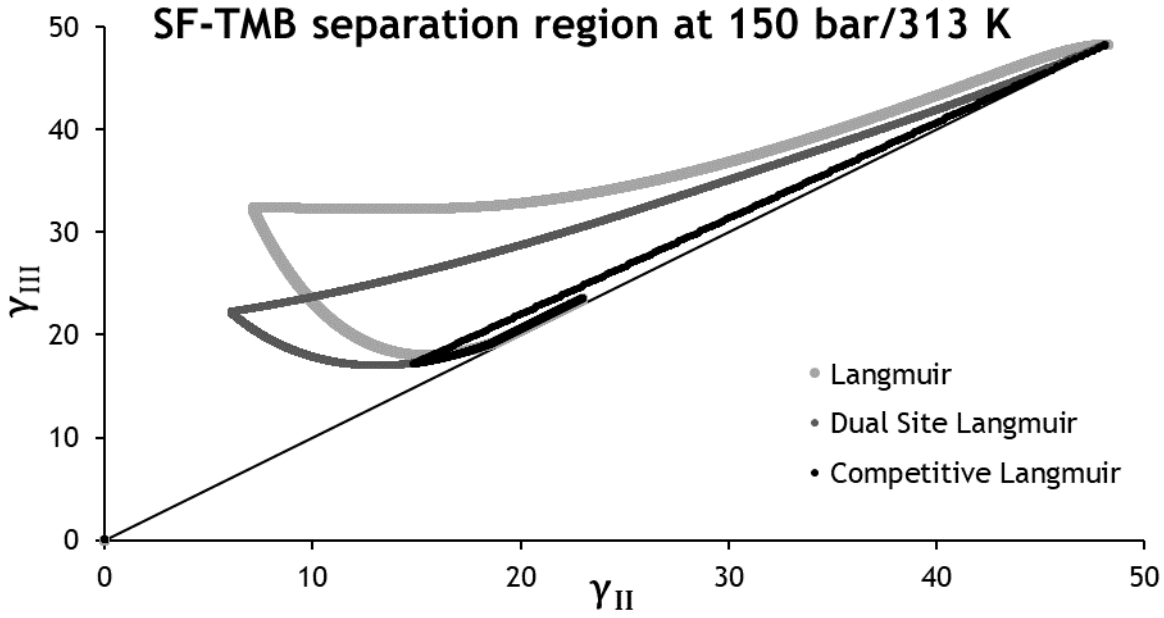

Figure 16 - Separation regions for the three scenarios at the reference operating conditions 150 bar /313 K. Parameters: β = 0.3; u_s = 0.75 cm min^{-1}; PUR_R and PUR_X > 99 %.

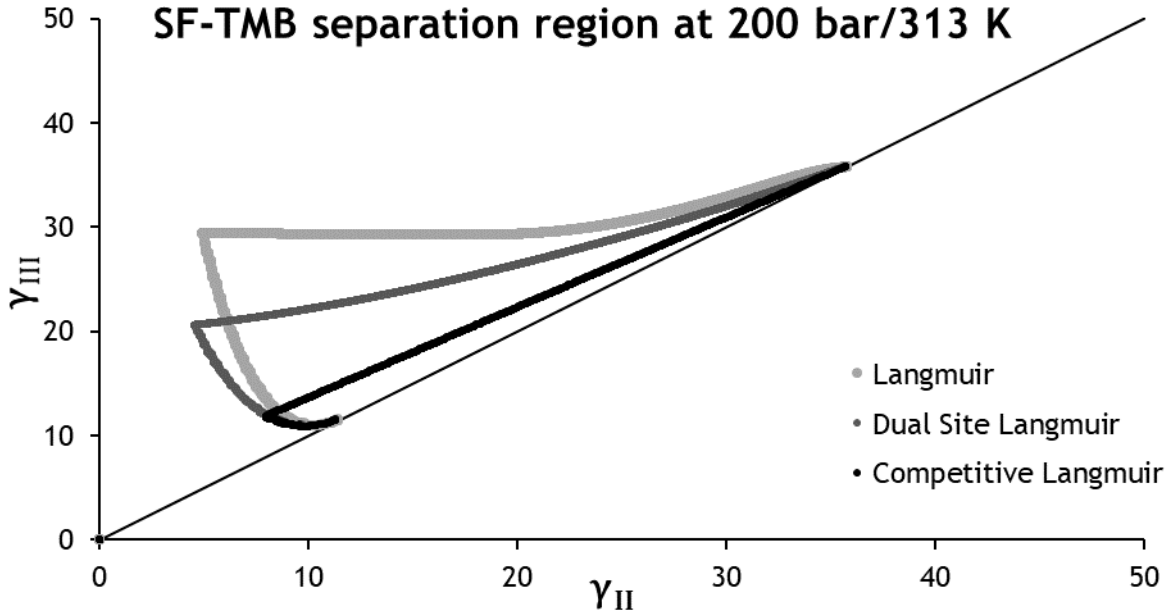

Figure 17 - Separation regions for the three water Langmuir adsorption models at the operating conditions 200 bar /313 K. Parameters: β = 0.2; u_s = 0.75 cm min^{-1}; PUR_R and PUR_X > 99 %.

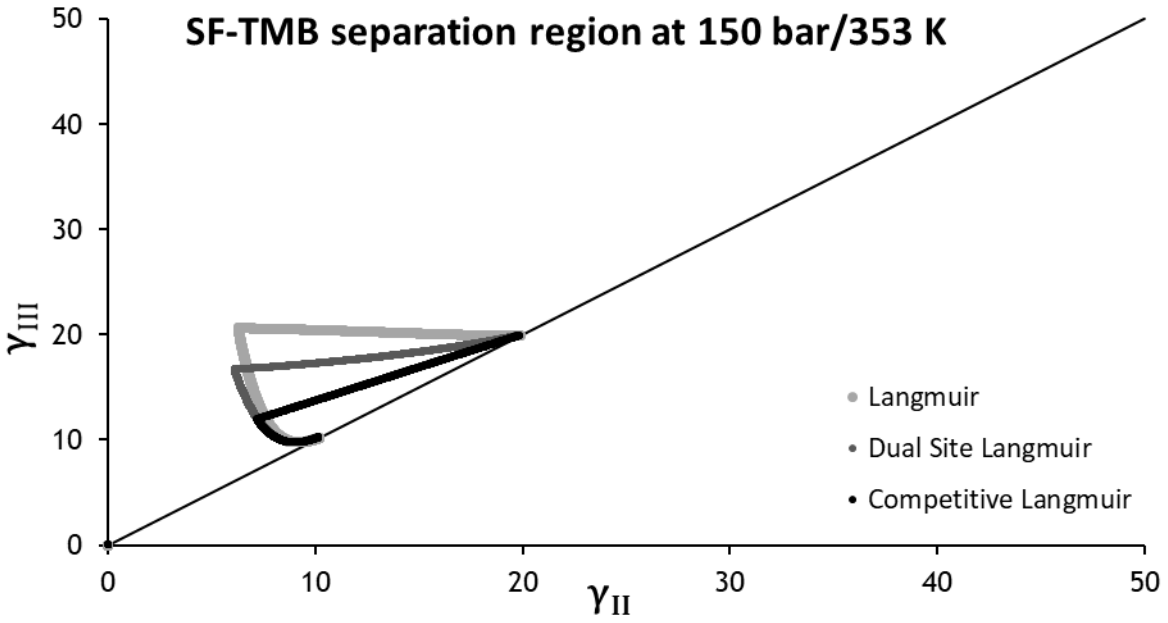

Figure 18 – Separation regions for the three water Langmuir adsorption models at the operating conditions 150 bar /353 K. Parameters: β = 0.4; u_s = 3.75 cm min^{-1}; PUR_R and PUR_X > 99 %.

Table 12 - **Performance parameters** for a 99% purity SF-TMB at three different operating conditions (150 bar /313 K; 200 bar /313 K; 150 bar /353 K), considering the three Langmuir adsorption isotherm model hypothesis.

Conditions	Langmuir adsorption isotherm model	PR_R $kg_{Solk}/(L_{Ads}\cdot day)$	DC_R L_{Des}/kg_{solk}
150 bar 313 K	Non-competitive	9.0	56.7
	Competitive	0.8	217.2
	Dual site competitive	5.8	76.0
200 bar 313 K	Non-competitive	8.8	39.8
	Competitive	1.4	108.8
	Dual site competitive	5.7	50.8
150 bar 353 K	Non-competitive	25.7	45.7
	Competitive	8.4	99.9
	Dual site competitive	18.8	56.1

In Figure 16 to Figure 18 it is possible to see that the separation regions are lay down to the left and different from the ideal triangle shape. The obtained separation regions are large enough to accommodate slight flow rate fluctuations without getting out of the separation region, which would lead to the contamination of the outlet streams.

In Appendix 5, some of the TMB internal concentration profiles are displayed.

A 18.8 kg_{solk}/L_{ads}·day productivity referent to the raffinate was found at 150 bar/353 K for the dual site Langmuir model (used as example since it provides intermediate competitive adsorption values). Despite the very low feed concentration, the productivity value was similar to the value found for other acetals production by SMBR [52] and slightly lower than for the production of dimethyl carbonate in a 24 columns SF-TMBR [11]. The eluent consumption values are quite high; however, this is a consequence of the low feed concentrations considered [11, 52].

Furthermore, one of the huge advantages of using CO_2 compared to other solvents relies on the easy separation from the products and easy of recycling, virtually with no losses. The eluent CO_2 is recycled just by depressurizing the stream. Both raffinate and extract streams comes out with the eluent CO_2 and to separate it from the products and reuse it, it is as simple as lowering the pressure below the 74 bar CO_2 critical pressure. Subcritical CO_2 become gaseous while solketal and water remains in the liquid stream as nonvolatile compounds and with low solubilities in subcritical CO_2. So, no complex and expensive processes so separate the product from the eluent are needed. Also, no complex equilibrium limitations are found, contrary to other processes were azeotropes mixtures are formed, leading to complex distillation or membrane processes to recover the eluent, complicating and increasing equipment and operation costs [27].

5 Conclusions

5.1 Objectives Achieved

The supercritical pulse experiences were successfully studied for all the proposed concentration and operating conditions. The exception goes for water pulses at 200 bar and 313 K and at 150 bar and 353 K for the loop of 200 µl, where flow and acquisition data problems were found. However, a lot of reproducibility problems were found, especially for low pressures (100 bar) and water pulses in any condition and concentration, requiring a huge amount of repetitions in order to achieve more precise and reliable data.

The pulse experience gave $\overline{t}_r$ values that follow the trends reported by Majewski et. al (2005) [10] for supercritical conditions: increasing the temperature results in the increasing of $\overline{t}_r$ and the opposite for pressure. For temperature, this tendency was reported for all acetone and solketal concentrations studied considering the limit temperatures tested, 313 and 353 K. The exception goes for water were the opposite behavior was found for all concentrations. Concerning the pressure, the $\overline{t}_r$ should decrease with increasing pressure, which was verified for all water pulse concentrations as well as solketal pulses from 150 to 200 bar, the most precise and reproducible experiences. At 100 bar the results have significant noise and low reproducibility. For acetone, contradictory tendency for different pulse concentrations and operating pressure was found concluding that pressure has almost no effect on acetone $\overline{t}_r$.

The global tendency of $\overline{t}_r$ reduction with increasing concentration and overlapping tails for the three compounds at all operating conditions supports the adjustment of equilibrium adsorption isotherms to a Langmuir model.

The LDF approximation provided a good fit of the pulse experiments after performing the required parameter estimation. Acetone, solketal and water pulses were successfully described by the model proposed using Langmuir adsorption isotherms. The values of k_L, K_{ads} and Q_{sat} were successfully predicted for all the compounds and concentrations studied at the most relevant operating conditions (150 and 200 bar, 313 and 353 K).

The TMB operating parameters were also successfully designed. Since multicomponent adsorption experiments could not be performed, three adsorption isotherm types were considered to study the multicomponent system: single component Langmuir isotherm (without competition), Competitive Langmuir isotherm and Dual Site Competitive Langmuir isotherm.

For a four 0.4x37.5 cm columns TMB with a minimum extract and raffinate purity of 99%, the best results were by far obtained at 150 bar and 353 K. Considering the Dual Site adsorption model, a solketal productivity of 18.8 kg_{Solk}/L_{Ads}·day and an eluent consumption of 56.1 $L_{Des}/kg_{solketal}$ was obtained. The results were found to be very promising comparing to the results obtained for similar processes described in the literature despite the low feed concentration considered.

5.2 Limitations and Future Work

Supercritical processes still have limited research and know-how, and the lack of information regarding several technical/scientific aspects is an issue. For instance, most of the traditional correlations, equations or studies found in literature may not be valid for supercritical conditions.

First, a most extensive study of phase equilibrium for glycerol, acetone, solketal and water in supercritical carbon dioxide is needed as well as experimental determination. For this, a different apparatus would be needed to handle high pressures and visual access to the system.

It should also be tested a wide range of operating conditions as supercritical fluids' properties are easily adjusted and tunable by changing operating conditions. Other supercritical fluids should be tested as eluent or as reagent itself, using acetone in supercritical state, removing the need to separate any added eluent, like it was proposed and reported by Royon et al. (2011) [6]. It is suggested to better explore this via probably using an acid catalyst to improve the low yield found. This catalyst might also be a dehydration agent that can handle the high critical acetone temperature, to remove water for the system and overcoming the reaction equilibrium limitation.

Solketal production may be a solution for crude glycerol valorization, so a more extensive work should be done using diverse types of crude glycerol as raw material in order to design a robust industrial process, as crude glycerol contain impurities like methanol and salts that need to be separated from the solketal.

Breakthrough experiments should also be done to verify zeolite HBEA-25 saturation for solketal and water, to study and validate Langmuir adsorption isotherms for higher concentrations. Also, multicomponent pulses and breakthrough curves should be studied to prove the competitive nature of sorption process, but some equipment changes and more working time are required. It should also be tested longer and larger SFC fixed bed columns to reduce mass transfer issues, but no laboratorial material was available for that and it was important to do both equilibrium and kinetic studies.

The results obtained with the SFC-TMB simulation should be used to design a more interesting SMB, that could be tested. The introduction of acetone in the feed stream should be taken into account to better simulate a real process.

To finish, other adsorbents should be tested, preferable catalyst with acid and dehydrating properties. Some tested catalysts, like zeolites among others, are reported in literature, showing excellent performances for solketal production at normal operating conditions, opening new possibilities for process intensification, like using a SFC-SMBR.

References

1. Trifoi, A.R., P.Ş. Agachi, and T. Pap, *Glycerol acetals and ketals as possible diesel additives. A review of their synthesis protocols*. Renewable and Sustainable Energy Reviews, 2016. **62**: p. 804-814.

2. United Nations Conference on Trade And Development, U., *The global biofuels market: Energy security, trade and development*. October, 2014.

3. Nanda, M.R., et al., *Catalytic conversion of glycerol for sustainable production of solketal as a fuel additive: A review*. Renewable and Sustainable Energy Reviews, 2016. **56**: p. 1022-1031.

4. *Biofuels Market*. 2014, International Institute for Sustainable Development.

5. Quispe, C.A., C.J. Coronado, and J.A. Carvalho Jr, *Glycerol: production, consumption, prices, characterization and new trends in combustion*. Renewable and Sustainable Energy Reviews, 2013. **27**: p. 475-493.

6. Royon, D., S. Locatelli, and E.E. Gonzo, *Ketalization of glycerol to solketal in supercritical acetone*. The Journal of Supercritical Fluids, 2011. **58**(1): p. 88-92.

7. Moity, L., et al., *Glycerol acetals and ketals as bio-based solvents: positioning in Hansen and COSMO-RS spaces, volatility and stability towards hydrolysis and autoxidation*. Green Chemistry, 2015. **17**(3): p. 1779-1792.

8. Yaws, C.L., *The Yaws Handbook of Physical Properties for Hydrocarbons and Chemicals: Physical Properties for More Than 54,000 Organic and Inorganic Chemical Compounds, Coverage for C1 to C100 Organics and Ac to Zr Inorganics*. 2015: Gulf Professional Publishing.

9. Liong, K., P. Wells, and N. Foster, *Diffusion in supercritical fluids*. The Journal of Supercritical Fluids, 1991. **4**(2): p. 91-108.

10. Majewski, W., E. Valery, and O. Ludemann-Hombourger, *Principle and applications of supercritical fluid chromatography*. Journal of liquid chromatography & related technologies, 2005. **28**(7-8): p. 1233-1252.

11. dos Santos, B.A.V., *Process Intensification in the Synthesis of the Green Chemical Dimethyl Carbonate*. 2014, Department of Chemical Engineering, Faculty of Engineering, University of Porto, Portugal.

12. Galy, N., et al., *Glycerol in subcritical and supercritical solvents*. Journal of Chemical Technology and Biotechnology, 2017. **92**(1): p. 14-26.

13. Fenghour, A., W.A. Wakeham, and V. Vesovic, *The viscosity of carbon dioxide*. Journal of Physical and Chemical Reference Data, 1998. **27**(1): p. 31-44.

14. Puiggené, J., M. Larrayoz, and F. Recasens, *Free liquid-to-supercritical fluid mass transfer in packed beds*. Chemical Engineering Science, 1997. **52**(2): p. 195-212.

15. Gupta, R.B. and J.-J. Shim, *Solubility in supercritical carbon dioxide*. 2006: CRC press.

16. Day, C.-Y., C.J. Chang, and C.-Y. Chen, *Phase equilibrium of ethanol+ CO2 and acetone+ CO2 at elevated pressures.* Journal of Chemical & Engineering Data, 1996. **41**(4): p. 839-843.

17. Esteban, J., et al., *Liquid-Liquid Equilibria for the System Acetone+ Solketal+ Glycerol at (303.2, 313.2, and 323.2) K.* Journal of Chemical & Engineering Data, 2014. **59**(9): p. 2850-2855.

18. Krishna, R., et al., *Liquid—liquid equilibrium in tihe system glycerol—water—acetone at 25° C.* Fluid phase equilibria, 1989. **45**(1): p. 115-120.

19. Grossmann, T. and J. Winkelmann, *Ternary diffusion coefficients of glycerol+ acetone+ water by Taylor dispersion measurements at 298.15 K. 3. Water-rich region.* Journal of Chemical & Engineering Data, 2007. **52**(2): p. 341-344.

20. Medina-González, Y., et al., *Phase equilibrium of the CO 2/glycerol system: Experimental data by in situ FT-IR spectroscopy and thermodynamic modeling.* The Journal of Supercritical Fluids, 2013. **73**: p. 97-107.

21. King, M., et al., *The mutual solubilities of water with supercritical and liquid carbon dioxides.* The Journal of Supercritical Fluids, 1992. **5**(4): p. 296-302.

22. Panagiotopoulos, A. and R. Reid, *High-pressure phase equilibria in ternary fluid mixtures with a supercritical component*. 1985, ACS Publications.

23. ZANETTE, A., et al., *DETERMINATION EQUILIBRIUM DATA LIQUID-VAPOR FOR HIGH PRESSURE SYSTEMS INVOLVING CARBON DIOXIDE+ SOLKETAL+ OLEIC ACID.* Blucher Chemical Engineering Proceedings, 2015. **1**(2): p. 14651-14658.

24. Nanda, M.R., et al., *A new continuous-flow process for catalytic conversion of glycerol to oxygenated fuel additive: Catalyst screening.* Applied Energy, 2014. **123**: p. 75-81.

25. Clarkson, J.S., A.J. Walker, and M.A. Wood, *Continuous reactor technology for ketal formation: an improved synthesis of solketal.* Organic process research & development, 2001. **5**(6): p. 630-635.

26. Silva, V.M. and A.E. Rodrigues, *Novel process for diethylacetal synthesis.* AIChE journal, 2005. **51**(10): p. 2752-2768.

27. Rodrigues, A.E. and V.M.T.M. Da Silva, *Industrial process for acetals production in a simulated moving bed reactor*. 2009, Google Patents.

28. Pereira, C.S., et al., *Multifunctional reactor for the synthesis of dimethylacetal.* Industrial & Engineering Chemistry Research, 2008. **47**(10): p. 3515-3524.

29. Graca, N.S., et al., *Analysis of the synthesis of 1, 1-dibutoxyethane in a simulated moving-bed adsorptive reactor.* Chemical Engineering and Processing: Process Intensification, 2011. **50**(11): p. 1214-1225.

30. Faria, R.P., et al., *Glycerol valorisation as biofuels: selection of a suitable solvent for an innovative process for the synthesis of GEA.* Chemical engineering journal, 2013. **233**: p. 159-167.

31. Sá Gomes, P. and A.E. Rodrigues, *Simulated Moving Bed Chromatography: From Concept to Proof-of-Concept.* Chemical Engineering & Technology, 2012. **35**(1): p. 17-34.

32. Miller, L., *Preparative enantioseparations using supercritical fluid chromatography*. Journal of Chromatography A, 2012. **1250**: p. 250-255.

33. Mazzotti, M., G. Storti, and M. Morbidelli, *Supercritical fluid simulated moving bed chromatography*. Journal of chromatography A, 1997. **786**(2): p. 309-320.

34. Yaws, C.L. and C. Gabbula, *Yaws" Handbook of Thermodynamic and Physical Properties of Chemical Compounds*. 2003: Knovel.

35. Nadykto, A.B. and F. Yu, *Uptake of neutral polar vapor molecules by charged clusters/particles: Enhancement due to dipole-charge interaction.* Journal of Geophysical Research: Atmospheres, 2003. **108**(D23).

36. McCusker, C.B.a.L.B. *Database of Zeolite Structures*. May 2017; Available from: http://www.iza-structure.org/databases/.

37. Theuerkauf, J., P. Witt, and D. Schwesig, *Analysis of particle porosity distribution in fixed beds using the discrete element method.* Powder Technology, 2006. **165**(2): p. 92-99.

38. *PSE: gPROMS software*. Available from: https://www.psenterprise.com/products/gproms.

39. Plaza, M., et al., *Propylene/propane separation by vacuum swing adsorption using Cu-BTC spheres*. Separation and purification technology, 2012. **90**: p. 109-119.

40. Rodrigues, A., *Simulated moving bed technology: principles, design and process applications*. 2015: Butterworth-Heinemann.

41. Sassiat, P.R., et al., *Measurement of diffusion coefficients in supercritical carbon dioxide and correlation with the equation of Wilke and Chang.* Anal. Chem.;(United States), 1987. **59**(8).

42. Funazukuri, T., C. Kong, and S. Kagei, *Effective axial dispersion coefficients in packed beds under supercritical conditions.* The Journal of supercritical fluids, 1998. **13**(1): p. 169-175.

43. Ruthven, D.M., *Principles of adsorption and adsorption processes*. 1984: John Wiley & Sons.

44. Chung, S. and C.Y. Wen, *Longitudinal dispersion of liquid flowing through fixed and fluidized beds.* AIChE Journal, 1968. **14**(6): p. 857-866.

45. Catchpole, O.J., R. Bernig, and M.B. King, *Measurement and correlation of packed-bed axial dispersion coefficients in supercritical carbon dioxide*. Industrial & engineering chemistry research, 1996. **35**(3): p. 824-828.

46. Tan, C.S. and D.C. Liou, *Axial dispersion of supercritical carbon dioxide in packed beds.* Industrial & engineering chemistry research, 1989. **28**(8): p. 1246-1250.

47. V. Talrose, E.B.S., A.A. Goncharova, N.A. Messineva, N.V. Trusova, M.V. Efimkina. *Acetone UV/VIS absorption*. "UV/Visible Spectra" in NIST Chemistry WebBook, NIST Standard Reference Database Number 69, Eds. P.J. Linstrom and W.G. Mallard, National Institute of Standards and Technology, Gaithersburg MD, 20899, doi:10.18434/T4D303 15/06/2017]; Available from: http://webbook.nist.gov/cgi/cbook.cgi?ID=C67641&Mask=400#UV-Vis-Spec.

48. V. Talrose, E.B.S., A.A. Goncharova, N.A. Messineva, N.V. Trusova, M.V. Efimkina,. *Solketal UV/VIS absorption*. "UV/Visible Spectra" in NIST Chemistry WebBook, NIST Standard Reference Database Number 69, Eds. P.J. Linstrom and W.G. Mallard, National Institute of Standards and Technology, Gaithersburg MD, 20899, doi:10.18434/T4D303 15/06/2017]; Available from: http://webbook.nist.gov/cgi/cbook.cgi?ID=C100798&Mask=400#UV-Vis-Spec.

49. Segelstein, D.J., *The complex refractive index of water*. 1981, University of Missouri--Kansas City.

50. Loughlin, K.F., *Water isotherm models for 4A (NaA) zeolite*. Adsorption, 2009. **15**(4): p. 337-353.

51. Guiochon, G., A. Felinger, and D.G. Shirazi, *Fundamentals of preparative and nonlinear chromatography*. 2006: Academic Press.

52. Rodrigues, A.E., C.S. Pereira, and J.C. Santos, *Chromatographic reactors*. Chemical Engineering & Technology, 2012. **35**(7): p. 1171-1183.

53. Petrovic, L.J. and G. Thodos, *Mass transfer in flow of gases through packed beds. Low Reynolds number region.* Industrial & Engineering Chemistry Fundamentals, 1968. **7**(2): p. 274-280.

54. Sherwood, T.K., R.L. Pigford, and C.R. Wilke, *Mass transfer*. 1975: McGraw-Hill.

55. Wakao, N. and T. Funazkri, *Effect of fluid dispersion coefficients on particle-to-fluid mass transfer coefficients in packed beds: correlation of Sherwood numbers*. Chemical Engineering Science, 1978. **33**(10): p. 1375-1384.

56. Stüber, F., et al., *Supercritical fluid extraction of packed beds: external mass transfer in upflow and downflow operation.* Industrial & Engineering Chemistry Research, 1996. **35**(10): p. 3618-3628.

57. Tan, C.-S., S.-K. Liang, and D.-C. Liou, *Fluid—solid mass transfer in a supercritical fluid extractor*. The Chemical Engineering Journal, 1988. **38**(1): p. 17-22.

Appendix 1 – Adsorbent characterization

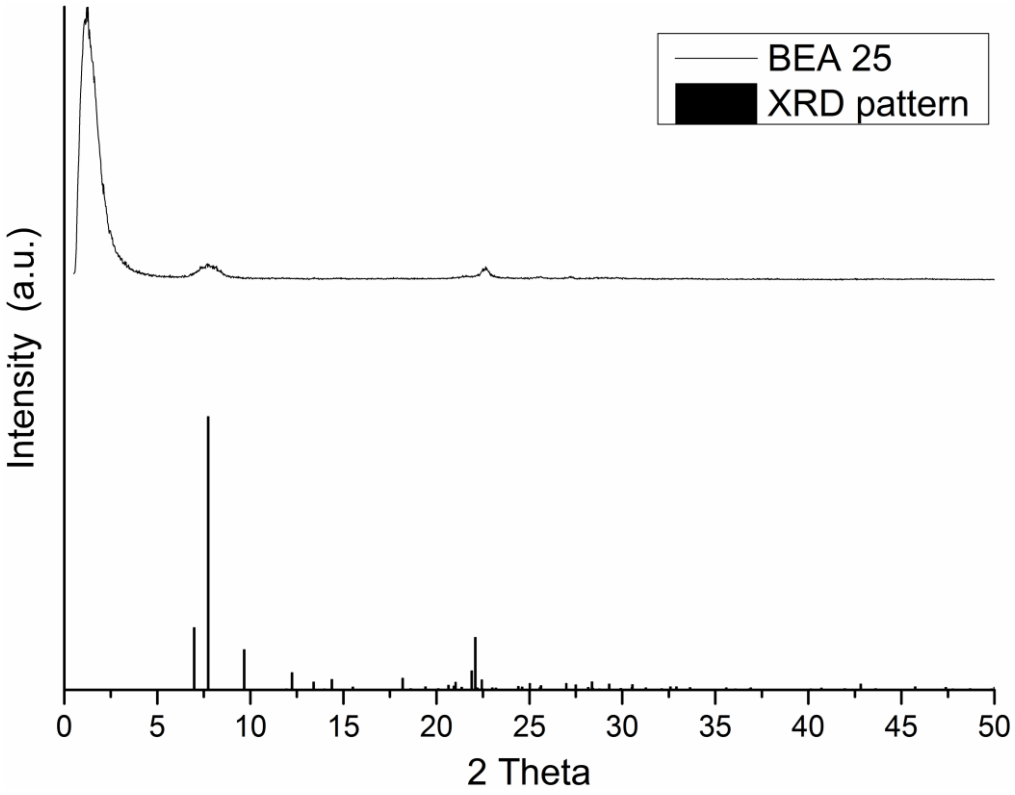

Figure A1.1– X-ray diffraction patterns of the zeolite HBEA-25: sample used in this work and IZA database (REF).

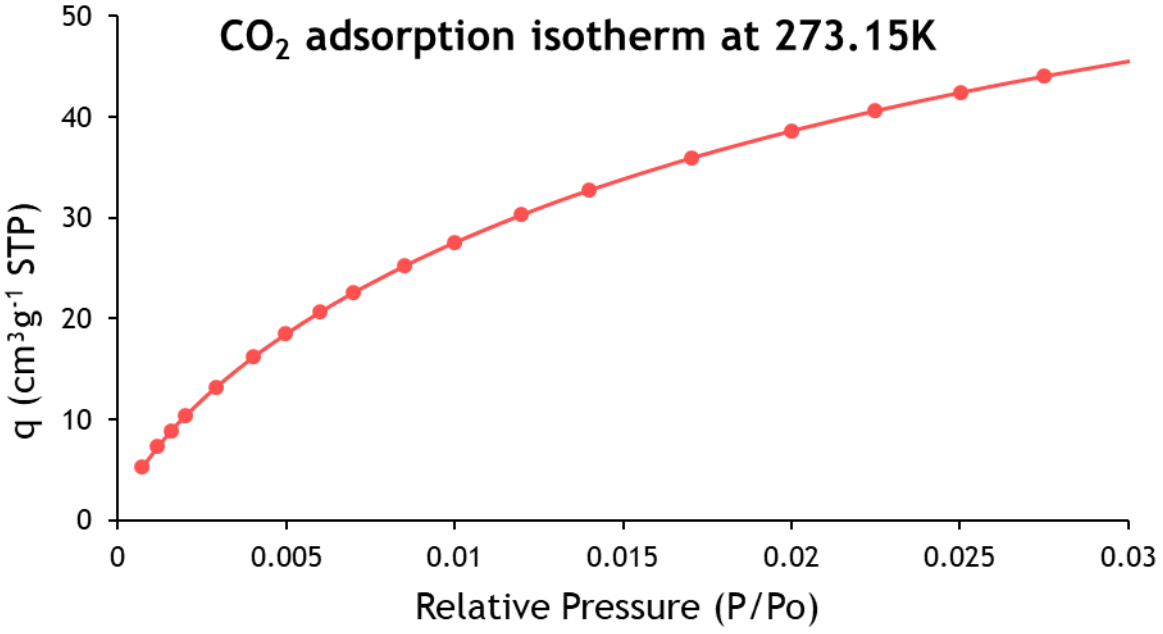

Figure A1.2– Zeolite HBEA-25 CO_2 adsorption equilibrium isotherm at 273.15K.

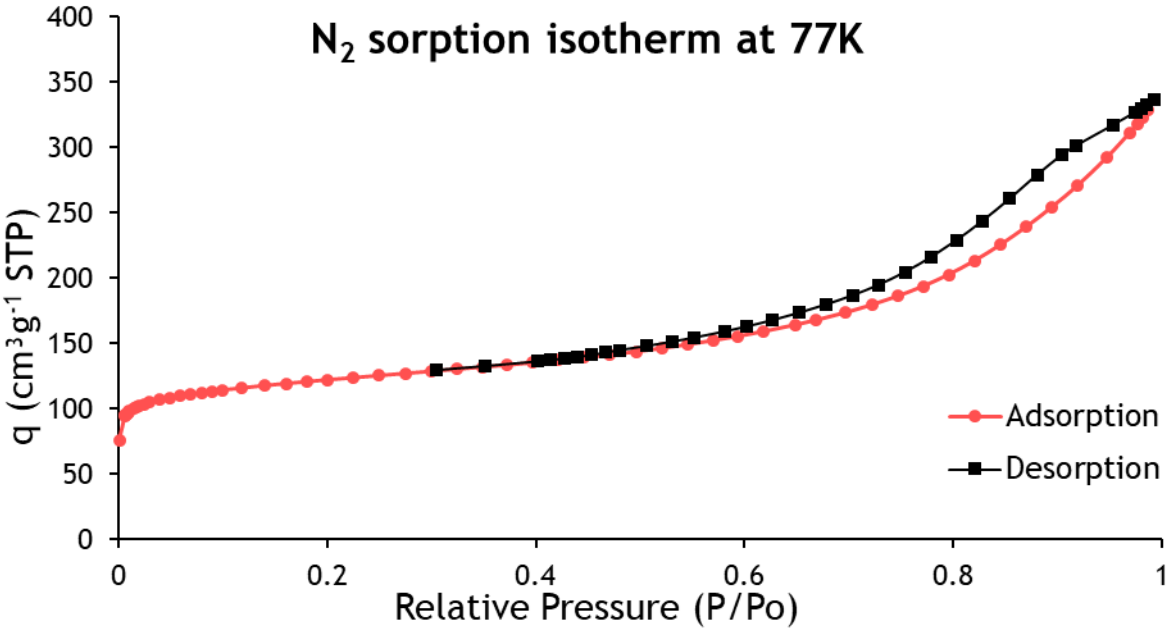

Figure A1.3 - Zeolite HBEA-25 N_2 adsorption equilibrium isotherm at 77K.

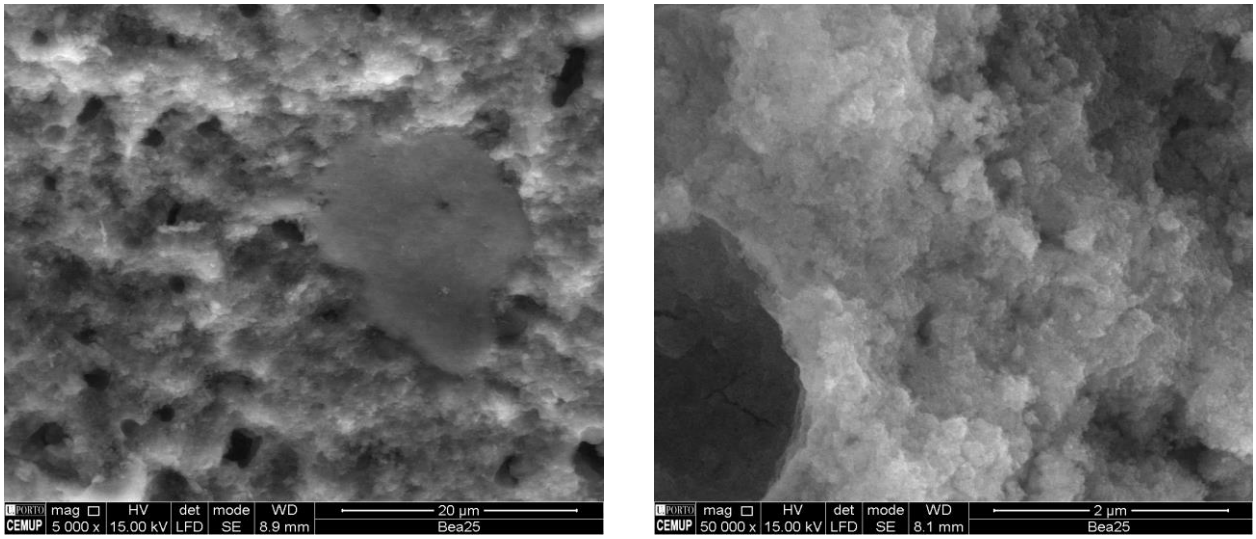

Figure A1.4 – SEM images of the zeolite HBEA-25 from Centro de Materiais da Universidade do Porto (CEMUP). The zoom on the right scan is 10 times higher than the left scan.

Appendix 2 – Waters' SFC-Unit

Figure A2.1 – SFC-FB unit from Thar/Waters. On the top it is a general view of the modular unit and on the bottom the oven where the fixed bed column is dispose.

Appendix 3 – UV/VIS spectrums

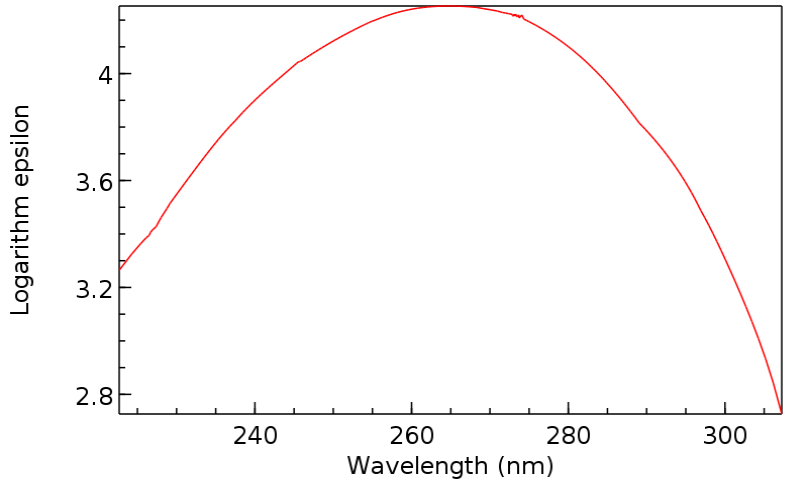

Figure A3.1 – Acetone UV/VIS absorption spectrum. Reprinted from [47].

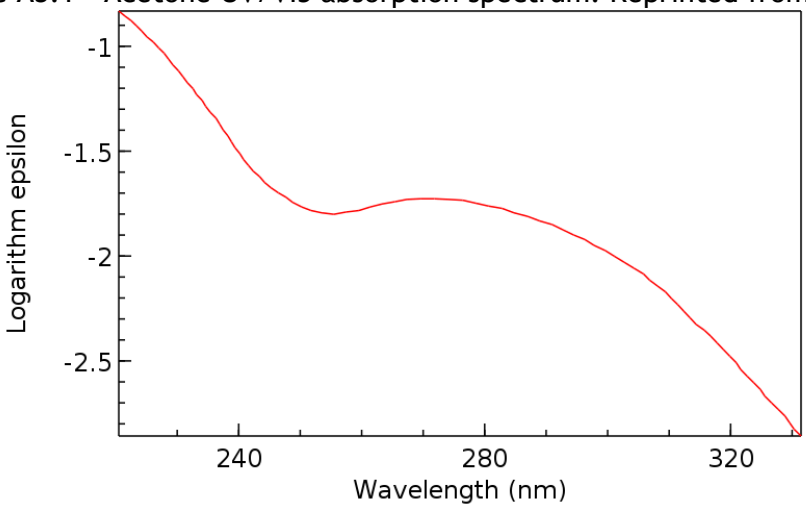

Figure A3.2 – Solketal UV/VIS absorption spectrum. Reprinted from [48].

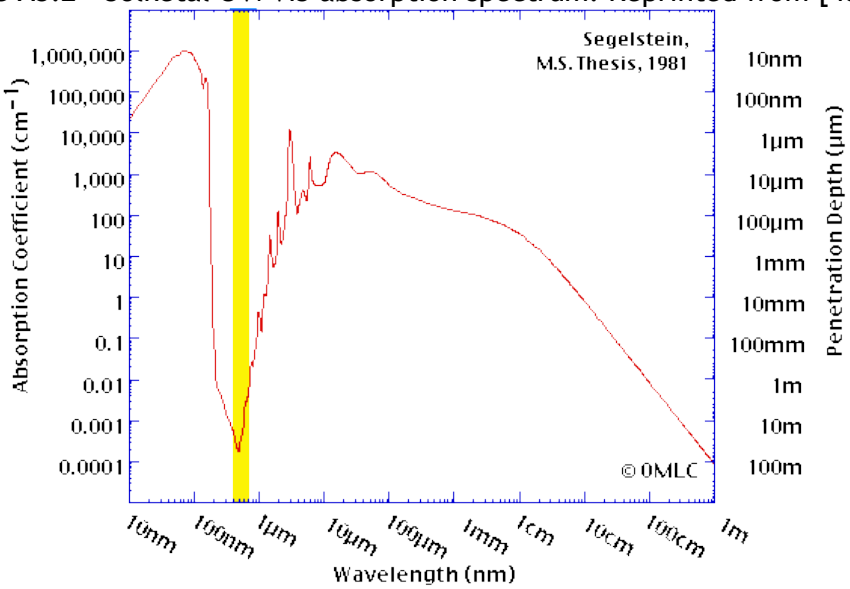

Figure A3.3 – Water UV/VIS absorption spectrum. Reprinted from [49].

Appendix 4 – Correlations for internal, external and global mass transfer coefficient

Global mass transfer coefficient

Assuming a liner driving force for the mass transfer from the bulk to the particle pores, the overall mass transfer coefficient (k_L) may take into account the external mass transfer coefficient (k_{ext}) and the internal mass transfer in the pores (k_{int}). Usually, it is assumed a resistance in series for the global mass transfer coefficient, given by equation (49) [11].

$$\frac{1}{k_L} = \frac{1}{k_{int}} + \frac{1}{k_{ext}} \tag{49}$$

Internal mass transfer coefficient

The k_{int} may be obtained by Glueckauf et al. correlation, described by equation (50). The effective diffusion coefficient D_{ef} may be obtained by equation (51). The particle tortuosity τ_p could be assumed as the typical value 2. [11]

$$k_{int} = \frac{5D_{ef}}{r_p} \tag{50}$$

$$D_{ef} = \frac{\varepsilon_p D_{12}}{\tau_p} \tag{51}$$

External mass transfer coefficient

The k_{ext} depends on the hydrodynamics of the system and is calculated by equations (52) or (53) using the Sherwood (Sh) or Stanton mass (St) dimensionless number.

Sh and St numbers can be predicted by several correlations for fixed bed columns available in literature, some of them described by equations (54) to (62), summarized in Table A3.1. All these correlations are functions of Reynolds (Re) and Schmidt (Sc) dimensionless numbers obtained by equations (37) and (38) respectively. Sh and St numbers are directly or indirectly functions of the operating temperature and pressure and D_{12}, turning them different for each compound and operating condition.

Notice that the correlations TanLiou, Puiggené et.al and Stüber et.al were obtained and tested for $ScCO_2$ through SFC-FB, the first two with non-porous particles and the last one with porous pellets with particles diameter about the same as the adsorbent HBEA-25 used in this work. As the correlations give a somewhat different values, the correlations designed tested for $ScCO_2$ are preferable.

$$Sh = \frac{k_{ext}\, d_p}{D_{12}} \quad (52)$$

$$St = \frac{k_{ext}}{u0} \quad (53)$$

Table A3.1 - Correlations for estimation of the external mass transfer coefficient (k_{ext}) in a fixed bed column through Sh or St number.

Authors	Correlation	Type of fluid and operation range	Eq.	Ref
Petrovic-Thodos	$Sh = \frac{0.357}{\varepsilon_b} Re^{0.64} Sc^{0.33}$	Gases; 2<Re<2000	(54)	[43, 53]
Kataoka	$Sh = 1.85 \left(\frac{1-\varepsilon_b}{\varepsilon_b}\right)^{1/3} Re^{1/3}\, Sc^{1/3}$	Liquids; Re<100	(55)	[51]
Wilson-Geankoplis	$Sh = \frac{1.09}{\varepsilon_b} Re^{0.33} Sc^{0.33}$ $Sh = \frac{0.25}{\varepsilon_b} Re^{0.69} Sc^{0.33}$	Liquids 0.0015<Re<55 55<Re<1050	(56)	[43]
Ranz-Marshall	$Sh = 2 + 0.6\, Re^{1/2} Sc^{1/3}$	Freely falling solid spheres	(57)	[43]
Sherwood-Pigford-Wilke	$St = 1.17\ Re^{-0.415} Sc^{-2/3}$	Gases and Liquids 10<Re<2500	(58)	[54]
Wakao-Funazkri	$Sh = 2.0 + 1.1 Re^{0.6} Sc^{1/3}$	Gases and Liquids 3<Re<104	(59)	[43, 55]
Puiggené-Larrayoz-Recasens	$Sh = 0.206\, Re^{0.80} Sc^{1/3}$	$ScCO_2$ through nonporous fixed bed 80<P<255 bar; 10<T<320 K	(60)	[14]
Stüber	$Sh = 0.269\, Re^{0.88} Sc^{0.33}$	$ScCO_2$ through sintered porous pellets of two sizes (dp of 1 and 2 cm) 8<Re<90	(61)	[56]
Tan-Liou	$Sh = 0.38\, Re^{0.83} Sc^{1/3}$	2<Re, Sc<40 $ScCO_2$ through nonporous fixed bed	(62)	[57]

Appendix 5 – SF-TMB internal concentration profiles

The following figures are the internal concentration profiles obtained by gPROMS's simulation, where the position 0 to 1 correspond to the column 1 dimensional axial position (z) and 1 to 2, 2 to 3, 3 to 4 corresponds to column 2, 3 and 4 respectively. The minimum PUR_R and PUR_X was set at 99 %.

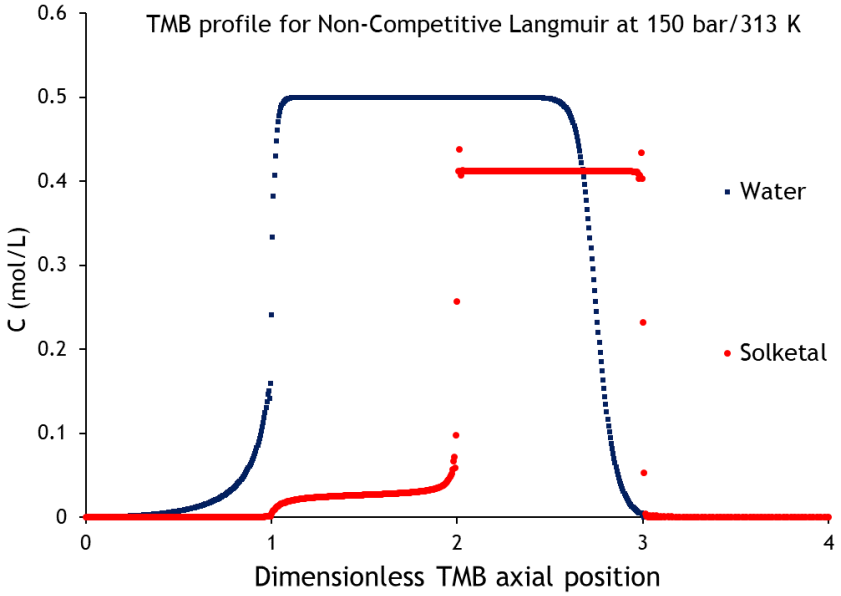

Figure A5.1 – SF-TMB internal concentration profile for a binary feed mixture of solketal and water at 150 bar/313 K considering Non-Competitive Langmuir Adsorption. β = 0.3; u_s = 0.75 cm min^{-1}.

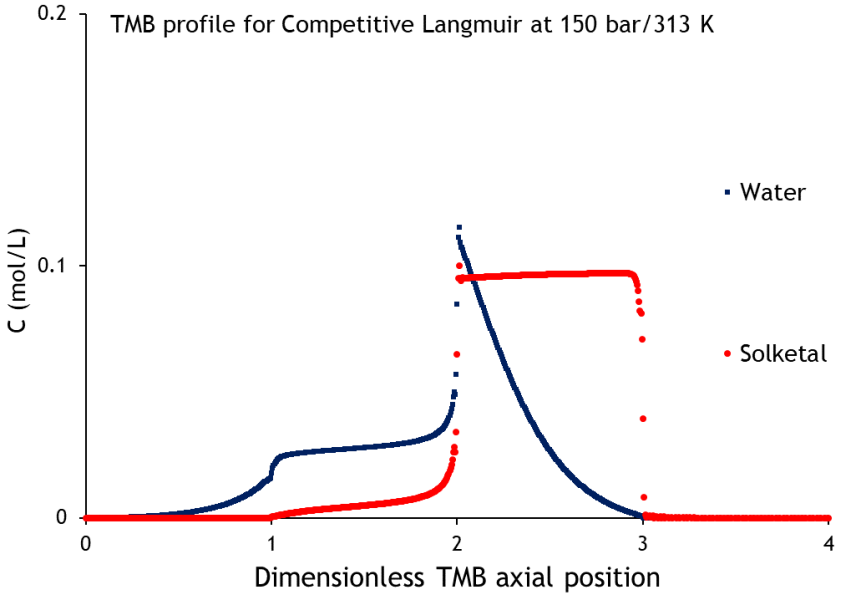

Figure A5.2 – SF-TMB internal concentration profile for a binary feed mixture of solketal and water at 150 bar/313 K considering Competitive Langmuir Adsorption. β = 0.3; u_s = 0.75 cm min-1.

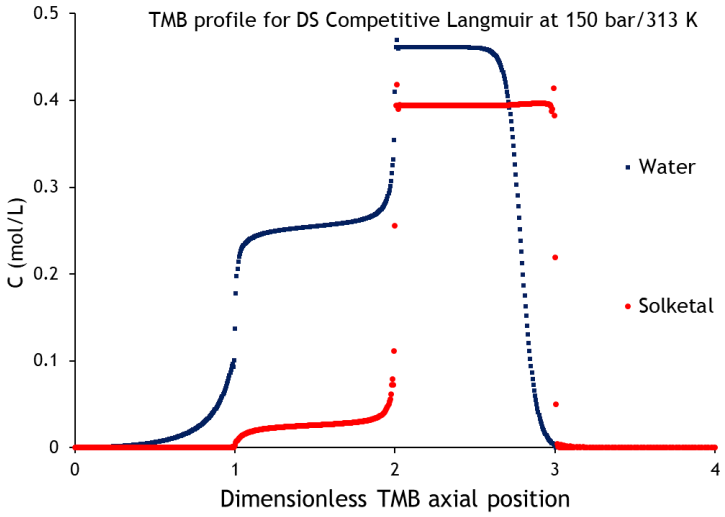

Figure A5.3 – SF-TMB internal concentration profile for a binary feed mixture of solketal and water at 150 bar/313 K considering DS Competitive Langmuir Adsorption. β = 0.4; u_s = 0.75 cm min^{-1}; α = 0.412.

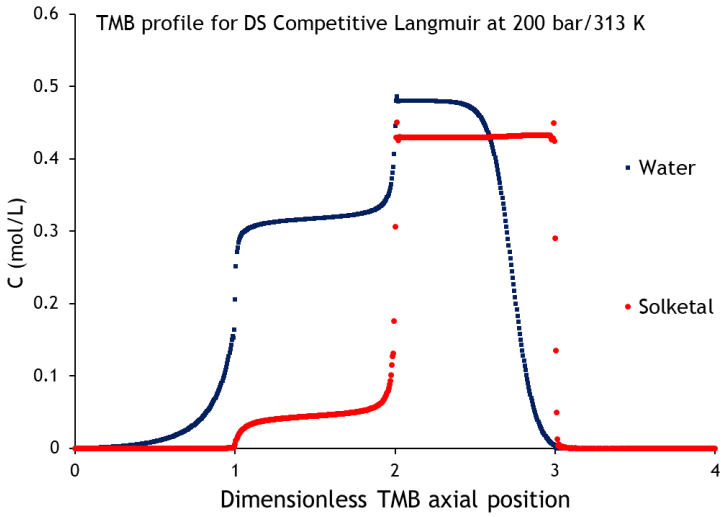

Figure A5.4 – SF-TMB internal concentration profile for a binary feed mixture of solketal and water at 200 bar/313 K considering DS Competitive Langmuir Adsorption. β = 0.2; u_s = 0.75 cm min^{-1}; α = 0.412.

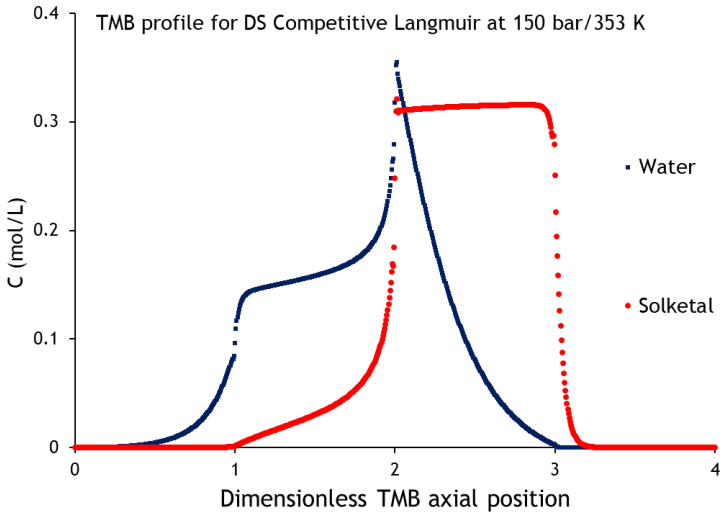

Figure A5.5 – SF-TMB internal concentration profile for a binary feed mixture of solketal and water at 150 bar/353 K considering DS Competitive Langmuir Adsorption. β = 0.4; u_s = 3.75 cm min^{-1}; α = 0.412.